Distinguishing evaporation-like and boiling-like modes of pseudo-boiling in supercritical pressures

Xiaotian He [a], Jinliang Xu [a,*], Xiongjiang Yu [b], Jian Xie [b]

[a] Beijing Key Laboratory of Multiphase Flow and Heat Transfer for Low Grade Energy Utilization, North China Electric Power University, Beijing 102206, China
[b] Key Laboratory of Power Station Energy Transfer Conversion and System of Ministry of Education, North China Electric Power University, Beijing 102206, China

ARTICLE INFO

ABSTRACT

In this study, we identify whether evaporation-like (EL) mode and boiling-like (BL) mode occur under supercritical pressures by investigating the heat transfer of platinum (Pt) and nickel-chromium (NiCr) wires, with a length of 22.0 mm and diameter of 70 μm, in carbon dioxide liquid at 8 and 10 MPa. Using a direct photographic technique based on the light refractive principle, we analyse the brighter/darker pattern in a varied-density field. The vapor–liquid interface is quantified using the grey extraction method. Our results show that beyond the limit of natural convection (NC), only the EL mode is identified for the Pt wire. However, for the NiCr wire, the EL mode, the transition from EL to BL (TEB) mode, and the BL mode are observed. The opposing gravity and drag forces cause downward bending of the Pt wire and upward bending of the NiCr wire. In the TEB region, the varying importance of interfacial expansion velocity over the buoyancy velocity accounts for the piston motion of the NiCr wire. During falling of the wire, the lighter fluid penetrating the heavier fluid causes interfacial instability to trigger the intermittent BL heat transfer. Beyond the TEB region, continuous BL heat transfer is observed. We introduce the small-perturbation theory to achieve a new non-dimensional parameter, H_3. For the Pt wire, a smaller (either negative or positive) H_3 explains why only the EL mode appears. For the NiCr wire, the negative H_3 in the TEB region proves that the intermittent BL heat transfer is caused by the piston motion of the wire, but the positive and ~30 times larger H_3 indicates that the continuous BL heat transfer is caused by the temporal-spatial temperature variations. Furthermore, we observe that the BL mode occurs in a vapor-like layer instead of wall cavities, which is different from subcritical boiling. The BL mode displays random and disordered features, like those of subcritical boiling. This work elaborately explores common and uncommon features between supercritical pseudo-boiling and subcritical boiling, and uncovers the secret of two modes of pseudo-boiling.

© 2023 Elsevier Ltd. All rights reserved.

1. Introduction

Supercritical fluid (SF) is a fluid under the condition of $P>P_c$ and $T>T_c$, where P and T are the pressure and temperature, respectively, and the subscript c refers to the critical point [1]. SFs are used in various applications, such as energy and power conversion [2,3], drug production [4], material fabrication [5], and chemical species preparation [6]. SFs are typically considered as single-phase fluids without bubbles, droplets, or interfaces [7]. However, significant deviations have been observed between correlations and measurements of supercritical heat transfer based on single-phase fluid theory [8–12]. For example, heat transfer deterioration, which

affects the safe operation of many industrial facilities, cannot be accurately predicted by single-phase fluid theory [13,14].

Pseudo-boiling was proposed in ~1960s [15,16]. To convert thermal energy into power using SF, convective heat transfer was studied in tubes under high heat flux conditions [17]. Under the conditions of high heat flux or low mass fluxes, wall temperatures were observed to have sharp peaks before the fluid reaches the pseudo-critical temperature [18], accompanying noise and flow instabilities [19]. Hence, the term "pseudo-boiling" refers to the heat transfer process in supercritical pressure which is similar to subcritical boiling.

Experiments were performed with heater wire immersed in pool liquid at near critical pressure. Knapp and Sabersky [20] observed three flow patterns: (1) free convection flow, (2) highly turbulent flow in which fluid aggregates like bubbles, and (3) os-

Nomenclature

Abbreviations

BL	boiling-like
EL	evaporation-like
GL	gas-like
LL	liquid-like
MC	micro-convection
ME	microlayer-evaporation
NC	natural convection
NiCr	nickel-chromium
Pt	platinum
SF	supercritical fluid
sCO_2	supercritical carbon dioxide
TC	transient conduction
TEB	transition from evaporation-like to boiling-like
TPL	two-phase-like
VL	vapor-like
A	coefficient related to polarizabilities (m^3/kg)
A_Ψ	amplitude of Ψ'
a	reference length in Fig. 20 (m)
C	grey level
$\hat{C}$	non-dimensional grey level
C_d	drag coefficient
c_1, c_2, c_3	correlated constant between $T*$ and $\delta *$
c_p	specific heat capacity (J/kg·K)
D	diameter of shadow area (μm)
d	diameter of wire (μm)
e_A, e_R, e_S	average, mean absolute and standard deviation
F_b	buoyancy force (N)
F_d	drag force (N)
F_p	contact pressure force (N)
F_{sL}	shear force (N)
F_{sy}	surface tension (N)
f_d	uniform load of drag force (N/m)
Gr	Grashof number ($\frac{g\beta\Delta T_{w,L}d^3}{\nu^2}$)
g	gravitational acceleration (m/s^2)
H_1, H_2, H_3	non-dimensional parameters in instability analysis
h	heat transfer coefficient (kW/m^2K)
I	current (A)
j_T	temperature coefficient of resistance (1/°C)
k	wave number of Ψ'
L	length of wire (mm)
l_{cl}	capillary length (m)
LP	light power (W)
mg	gravity force per unit length (N/m)
n	refractive index
n_0	refractive index of the fibre
P	pressure (MPa)
Pr	Prandtl number (ν/α_T)
q	heat flux (W/m^2)
Q	heating power (W)
R	electrical resistance
Re	Reynolds number ($\frac{\rho vd}{\mu}$)
r	radius (m)
s	cross-section area of wire (m^2)
T	temperature (°C)
DT	superheat (°C)
$\bar{T}*$	steady value of $T*$
$T*'$	perturbation value of $T*$
t	time (s)
U	voltage (V)

u	intermediate variable $u=rn(r)$
vb	velocity of buoyancy (m/s)
ve	velocity of expansion (m/s)
x, y, z	coordinate axis
$\hat{z}$	non-dimensional value of z
Δz	vertical displacement of wire

Greek symbols

α	deflection angle (°)
$\hat{\alpha}$	non-dimensional deflection angle
α_L	coefficient of linear expansion (1/K)
α_T	thermal diffusivity (m^2/s)
β	coefficient of thermal expansion (1/K)
β_T	volume coefficient of expansion (1/K)
δ	thickness (μm)
δ_{th}	thickness of thermal boundary layer (m)
δ_v	thickness of velocity boundary layer (m)
Φ_{int}	reference thermal property
Γ_0	incident light intensity (cd)
Γ_R	reflected light intensity (cd)
γ	Euler's constant
κ	scale factor between light intensity and voltage
λ	thermal conductivity (W/m·K)
μ	dynamic viscosity (Pa·s)
ν	kinematic viscosity (m^2/s)
Θ	heat source (W/m^3)
$\overline{\rho}$	electrical resistivity (Ω·m)
ρ	density (kg/m^3)
σ	surface tension (N/m)
ζ	non-dimensional perturbation propagation velocity
$\hbar$	enthalpy (kJ/kg)

Subscripts/Supercripts

air	in air
b	bulk
c	at critical condition
g	measured by fibre
IF	interface
L	average value on the whole wire
max/min	maximum and minimum
Pt	platinum
pc	pseudo-critical
ref	reference
s	standard resistance
sig	signal
start	start of pseudo boiling
t	total
term	terminal of pseudo boiling
w	wall
*	non-dimensional parameter

cillating flow where the free convection flow alternated with the bubble-like pattern. In Hahne and Neumann [21], laminar flow was observed for platinum wires, but three patterns of laminar flow, oscillatory flow, and turbulent film flow were found for nickel-chromium (NiCr) wires. The boiling-like (BL) characteristic may be attributed to the oscillatory and turbulent film regimes accompanying the bubble-like structures and high heat transfer coefficients. Neumann and Hahne [22] reported conventional free-convection heat transfer when using a platinum wire in a pool of liquid CO_2, in which bubble-like pattern was not observed. Tamba et al. [23] observed abnormal convection slightly above the critical point, which has been called the BL pattern. Their observations showed a transition from boiling at subcritical pressures to ordinary free convection far above the critical pressure. The analysis of

critical heat flux showed that the phenomenon gradually changes from boiling to free convection when pressure increases. Boiling disappears when the pressure is slightly higher than the critical pressure. In another study by Tamba et al. [24], an interface-like phenomenon was observed during heat transfer in argon near the critical point using molecular dynamics (MD) simulations. MD simulations at supercritical pressure reproduced a structure similar to the normal liquid–vapor interface at subcritical pressure when temperature gradient exists. The characteristics of the interface-like phenomenon, such as the density profile, interface thickness, and interfacial tension, were compared with those at subcritical pressures.

The transition from liquid-like (LL) fluid to gas-like (GL) fluid was considered theoretically when crossing the Widom line, which is the connection between series of points at which the specific heat or thermal expansion coefficient reaches maximum [25]. The P-T domain is divided into a GL region and a LL region by crossing the Widom line. MD simulations have shown that fluid structures are quite different in the GL and LL regions [26]. Banuti [27] developed transition temperature to cross the Widom line using a thermodynamic approach. The energy added to SF can be decoupled into two parts [27]. One part increases its temperature, acting as sensible heat, and the other part overcomes the intermolecular attraction, acting as a function like latent heat at subcritical pressure [27]. Using neutron imaging techniques, Maxim et al. [28] monitored the density fluctuations of supercritical water as the system evolved rapidly from the LL region to the GL region when crossing the Widom line during isobaric heating. Their observations showed that the Widom line of water could be identified by the neutron imaging techniques [28,29].

The Widom line method indicates that a SF is either LL fluid or GL fluid, depending on P and T. On the contrary, Ha et al. [30] reported the direct classification of LL and GL molecules coexisting in SF, as identified by machine learning analysis of simulation data. The deltoid coexistence region encloses the Widom line and may, therefore, be termed as the Widom delta. The number fractions of GL and LL particles were found to undergo continuous transitions across the delta following a simplified two-state model, suggesting a microscopic view of the SF as a mixture of LL and GL structures [30]. Xu et al. [31] simulated argon (Ar) in supercritical pressures. Three regimes were identified including the LL regime, GL regime, and TPL (two-phase-like) regime. The TPL regime contains nano-voids, inside which particles are sparsely distributed to achieve gas density, and outside which particles are densely populated to achieve liquid density. Voids have a curved interface like bubbles in subcritical pressures [31]. Voids in the supercritical state are called as "bubble-like" structure.

The literature survey on pseudo-boiling reveals several limitations in available studies. Firstly, most experiments were conducted near the critical pressure P_c [20–23,32], leading to the doubt that bubble-like pattern may not actually occur in supercritical pressures owing to measurement uncertainty. Secondly, while snapshot images show bubble-like flow or turbulent flow, the dynamic processes of these phenomena have not been presented [20–23]. Thirdly, most studies used the schlieren or shadowgraph method to capture images, which highlights fluid density gradients [20–22], but this method reduces image brightness and clarity after the light passes through the lens set, resulting in blurred boundaries between the LL fluid and the GL fluid and limiting the recording rate of pictures.

Now that heat transfer in subcritical pressures and supercritical pressures has similarities, an important question arises that can the two modes of heat transfer of evaporation and boiling in subcritical pressures, also take place in supercritical pressures? If so, what are the triggering mechanisms for the two modes of heat transfer, and what are the differences between them? To answer these questions, let us review evaporation and boiling in subcritical pressures. According to Kandlikar [33], "*Boiling is a phase change process in which vapor bubbles are formed either on a heated surface and/or in a superheated liquid layer adjacent to the heated surface. It differs from evaporation at predetermined vapor/gas-liquid interfaces, as it also involves creating these interfaces at discrete sites on the heated surface*". Boiling involves the nucleation and growth of bubbles, which can overcome the free energy barrier arising from the formation of a two-phase interface. However, evaporation transforms liquid into gas, which is usually barrierless when a macroscopic vapor–liquid interface exists in the system [34]. Two key differences exist between evaporation and boiling [7]. The first difference is where the change in state occurs. Evaporation occurs only at the surface of a liquid, whereas boiling may occur throughout the liquid. The second difference concerns the temperature. Evaporation occurs at any temperature, but boiling occurs only at the boiling point of the liquid.

The objective of this study is to investigate the two modes of heat transfer in supercritical pressures. Unlike other studies, the originalities of the present paper lie in the following: (1) Direct visualisation of pseudo-boiling is achieved using a high-speed camera without loss of brightness and clarity of the images. (2) An optical fibre detects high-frequency temperature variations that cause less disturbance to the flow field. (3) Synchronous measurements are conducted by connecting the electric and optical signals. (4) The interface adjoining the vapor-like (VL) and LL structures is quantitatively defined and determined experimentally for the first time. (5) The strong coupling between dynamics of the heater wire and flow field is analysed. New experimental results with two wires immersed in a pool of liquid CO_2 are reported, identifying only the EL mode for the Pt wire, but both the EL mode and the BL mode for the NiCr wire. The triggering mechanisms of the two modes of pseudo-boiling heat transfer using the NiCr wire are explored.

2. Experiments and methods

2.1. Two heater wires

Two wires were used, including a NiCr wire and a Pt wire. For the NiCr wire, Fig. 1(a) shows the scanning electron microscopy (SEM) image using a Zeiss Merlin (Germany), and Fig. 1(b) and (c) show the 3D morphology of the wire surface using a Bruker Contour GT-K (USA). The wire had a length of 22 ± 0.5 mm and a diameter of 70 ± 2 μm. The surface was very smooth, with an average roughness of 113.1 nm. Micro cavities were observed on the surface with a depth of 800 nm (Fig. 1d). Identical lengths and diameters were used for the Pt wire (Fig. 2). The Pt surface was smoother than the NiCr surface, with an average roughness of 11.4 nm. No cavities were observed on the Pt surface. Table 1 summarises the physical properties of the NiCr and Pt wires at room temperature.

The two wires were used not only for heaters to provide heat flux, but also for temperature sensors. A careful calibration determined the linear curves of the electric resistance and temperature for each wire. During the calibration, the wires were immersed in a liquid pool of silicon oil. The oil was well controlled at different temperatures with an uncertainty of 0.5°C. A constant DC voltage was applied to the wire, yielding different DC currents flowing through the wire, corresponding to different oil temperatures. Note that the current should be as low as 3 mA, ensuring that the temperature difference between the wire and the oil is smaller than 0.1°C. Hence, the wire temperature (T_w) can be regarded as the oil temperature owing to its negligible temperature difference. Fig. 3(a) shows the calibration results for the Pt
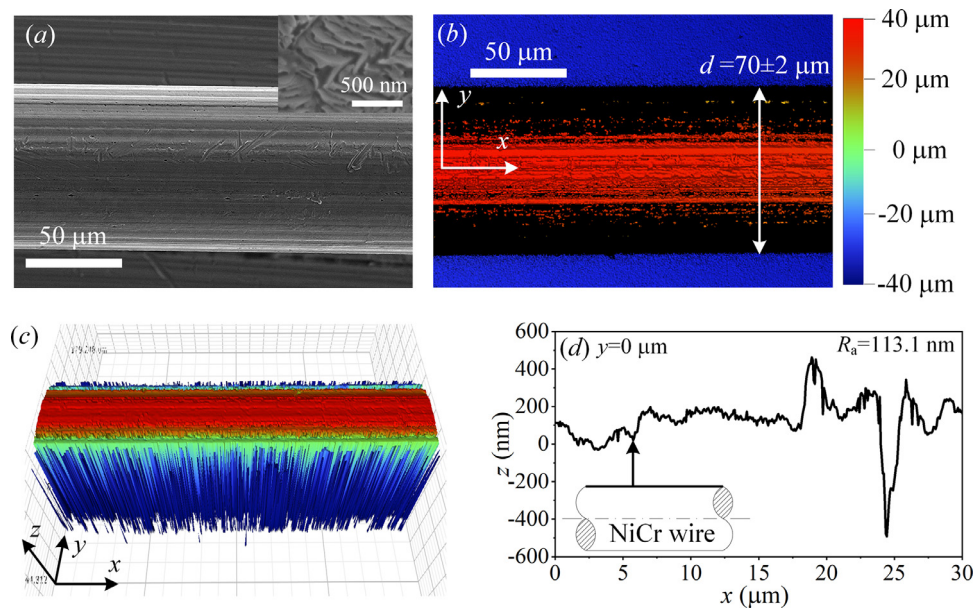
Fig. 1. Characterization of the NiCr wire. (*a*) SEM picture of the wire; (*b*) 3D morphology of the wire; (*c*) 3D morphology for the top region of the wire; (*d*) roughness on the wire surface.
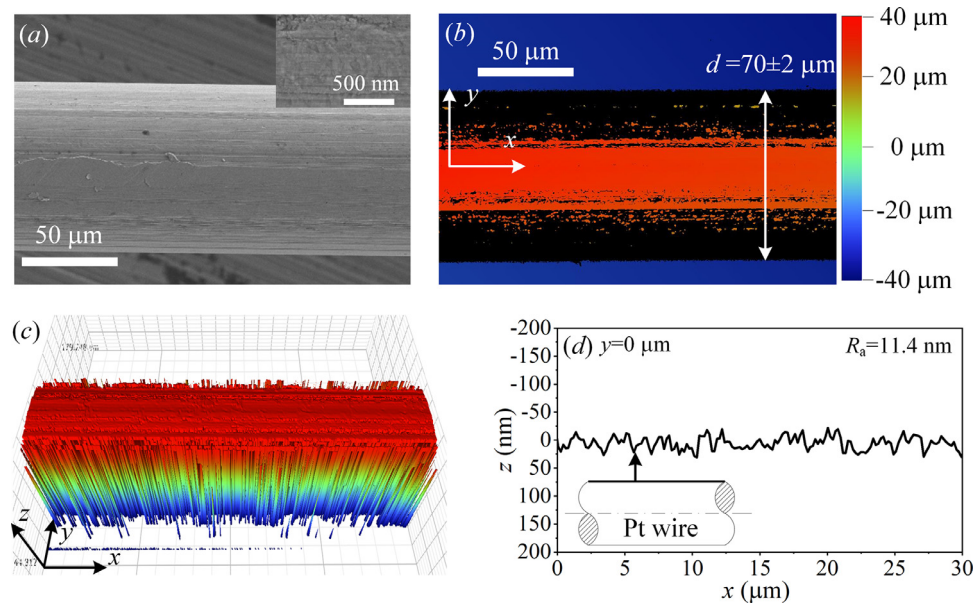
Fig. 2. Characterization of the Pt wire. (*a*) SEM picture of the wire; (*b*) 3D morphology of the wire; (*c*) 3D morphology for the top region of the wire; (*d*) roughness on the wire surface.

Table 1
Physical properties of Cr20Ni35 wire and Pt wire at 25°C and 1 atm.

Material	Density ρ (kg/m³)	Specific heat capacity $c_{p,w}$ (kJ/kg·K)	Thermal conductivity λ_w (W/(m·K))	Thermal diffusivity α_T (m/s)
Cr20Ni35	7900	0.50	13.0	0.82
Pt	21350	0.135	71.6	4.53

wire. The measured specific resistance of the Pt wire ($\bar{\rho}_{Pt}$) deviates from the standard values [35] by less than 0.63%, ensuring accurate calibration. The two calibration curves are shown as follows (see Fig. 3).

$$\bar{\rho}_{Pt} = 1.078 \times 10^{-7} \times \left(1 + 3.908 \times 10^{-3} T_w\right) \quad (1)$$

$$\bar{\rho}_{NiCr} = 1.106 \times 10^{-6} \times \left(1 + 4.216 \times 10^{-4} T_w\right) \quad (2)$$

2.2. Experimental setup

To study the heat transfer of NiCr and Pt wires in liquid CO_2, an experimental setup was established, including a high-pressure vessel, a pressure control system, a fibre optic measurement system, a high-speed camera, and a high-speed data acquisition system (see Fig. 4a). The horizontally positioned pressure vessel was made of 304 stainless steel with an inner diameter of 100 mm
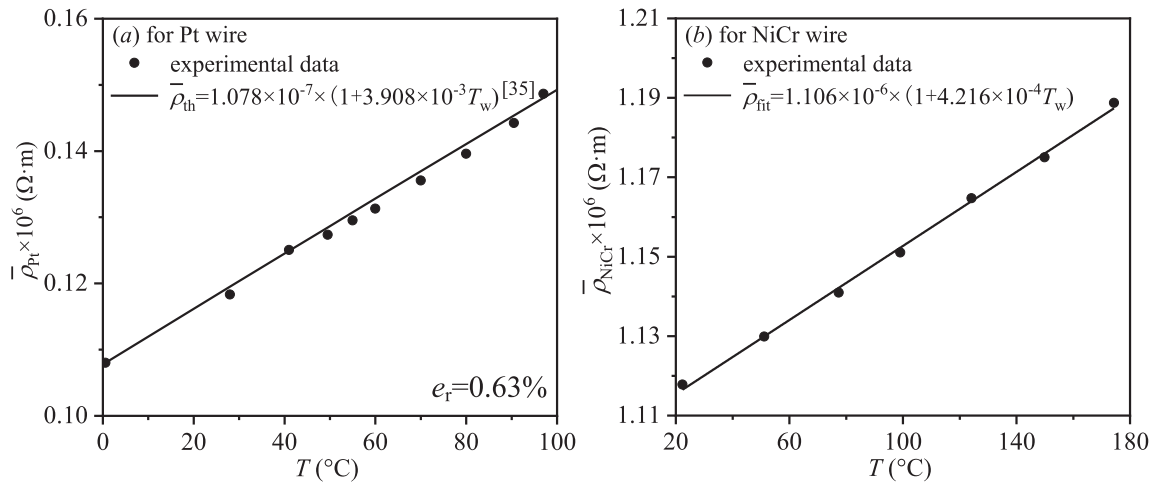
Fig. 3. Calibration of the specific resistances of the two wires. (*a*) for the Pt wire; (*b*) for the NiCr wire.

and a length of 140 mm (see Fig. 4*b*). Two sapphire glass windows were installed on the left-side and the right-side surfaces of the pressure vessel, each having a thickness of 15 mm. The pressure control system was connected with the top of the pressure vessel through a supercritical carbon-dioxide (sCO$_2$) inlet/outlet tube, which was used to remove non-condensable gas from the vessel (vacuum function), charge the CO$_2$ liquid into the vessel, and control the system pressure. During the experiment, the wire heating would cause increase in CO$_2$ temperature. Hence, a helical coiled tube of copper was installed in the pressure vessel. A circulating water with controlled flow rate and temperature flowed inside the helical coiled tube to maintain a constant temperature of the pool liquid in the pressure vessel (see Fig. 4*b* and *c*). The helical coiled tube penetrated the pressure vessel through the front and rear cylinder surfaces. A jacket thermocouple penetrated the front of the pressure vessel. Both the helical coiled tube and the thermocouple were sealed using ferrule tube fittings. The heater wire was positioned horizontally and perpendicular to the axial direction of the pressure vessel. The wire was connected to an external electric circuit to act as a heat source and a temperature sensor. Because the wire was tightly fixed by the two electrodes through which the DC voltage was applied, the wire was straight without bending at room temperature (see Fig. 4*d*). The fibre optic was positioned vertically in the pressure vessel. The tip of the fibre was (200±5) μm above the wire. A screw thread was machined onto the outer shell of the fibre. Thus, the relative distance between the fibre tip and the heater wire could be adjusted precisely. After the experimental setup was assembled, a hydrodynamic test of the entire system was performed to ensure no leakage.

The pressure control system is illustrated in Fig. 5. Initially, a vacuum pump was operated to remove the non-condensable gas from the closed system to a desired vacuum pressure. The pressure vessel was separated from the vacuum loop by a valve. An air compressor drove a piston pump to elevate the pressure from 5.5 MPa in the CO$_2$ gas bottle to 15 MPa, and pumped the CO$_2$ stream into the pressure vessel via a pressure-release valve and filter. The charged CO$_2$ in the pressure vessel was transformed into liquid because of the cooling of the circulating water via the helical coiled tube. If the pressure exceeded the desired value, the release valve at the top of the pressure vessel was opened to adjust the pressure. Fig. 6 shows the control outcomes for the pressure and temperature. For the desired pressure of 8 MPa and bulk fluid temperature of 15°C, the real values are controlled to (7.962∼8.025) MPa and (14.9∼15.0)°C, respectively, in a time period of 50 s.

2.3. Measurement system and parameter definition

2.3.1. Parameters for electric circuit

Here, we describe the measurement system, including the electric circuit, fibre optic, and image capture (see Fig. 7*a*). A DC voltage source (Itech 6132 B, China) supplied heating power to the heater wire with a voltage resolution of 0.1 mV and an accuracy of 0.02%. In the electric circuit, a standard resistance 14 with R_s= (8±0.03) Ω was connected in series with the heater wire. The DC voltage applied to the standard resistance and the heater is denoted by U_t, whereas that applied to the standard resistance alone is denoted by U_s. Hence, the heater resistance R_L and heating power Q_L applied to the heater are calculated in Eqs. (3) and (4), noting the time-dependent U_t and U_s, where t is the time.

$$R_L(t) = \frac{U_t(t) - U_s(t)}{U_s(t)} R_s \tag{3}$$

$$Q_L(t) = \frac{U_t(t) - U_s(t)}{R_s} U_s(t) \tag{4}$$

The heat flux based on the outer heater surface area is

$$q_L(t) = \frac{1}{\pi dL} \frac{U_t(t) - U_s(t)}{R_s} U_s(t) \tag{5}$$

and the specific resistance of the heater wire is

$$\bar{\rho}_L(t) = \frac{\pi d^2}{4L} \frac{U_t(t) - U_s(t)}{U_s(t)} R_s \tag{6}$$

The heater wire temperature $T_{w,L}$ at time t can be determined using Eq. (6) incorporating the calibration results of Eqs. (1) and (2), where d and L are the diameter and the length of the heater wire, respectively (d=70 μm and L=22 mm). The heat transfer coefficient h_L is calculated as follows:

$$h_L(t) = \frac{q_L(t)}{T_{w,L}(t) - T_b} \tag{7}$$

2.3.2. Fibre optic measurement

To capture temperature variations in the ∼μs timescale, a fibre optic was introduced, which has a faster response than thermocouples. This technique was initially applied by Avdeev et al. [36] to monitor the refractive index and density changes in supercritical fluids; however, temperature measurements using this technique in SF have not been reported previously. After being emitted by a light source, a laser beam with a wavelength of 1310 nm was divided by a splitter into a signal stream and a reference stream,
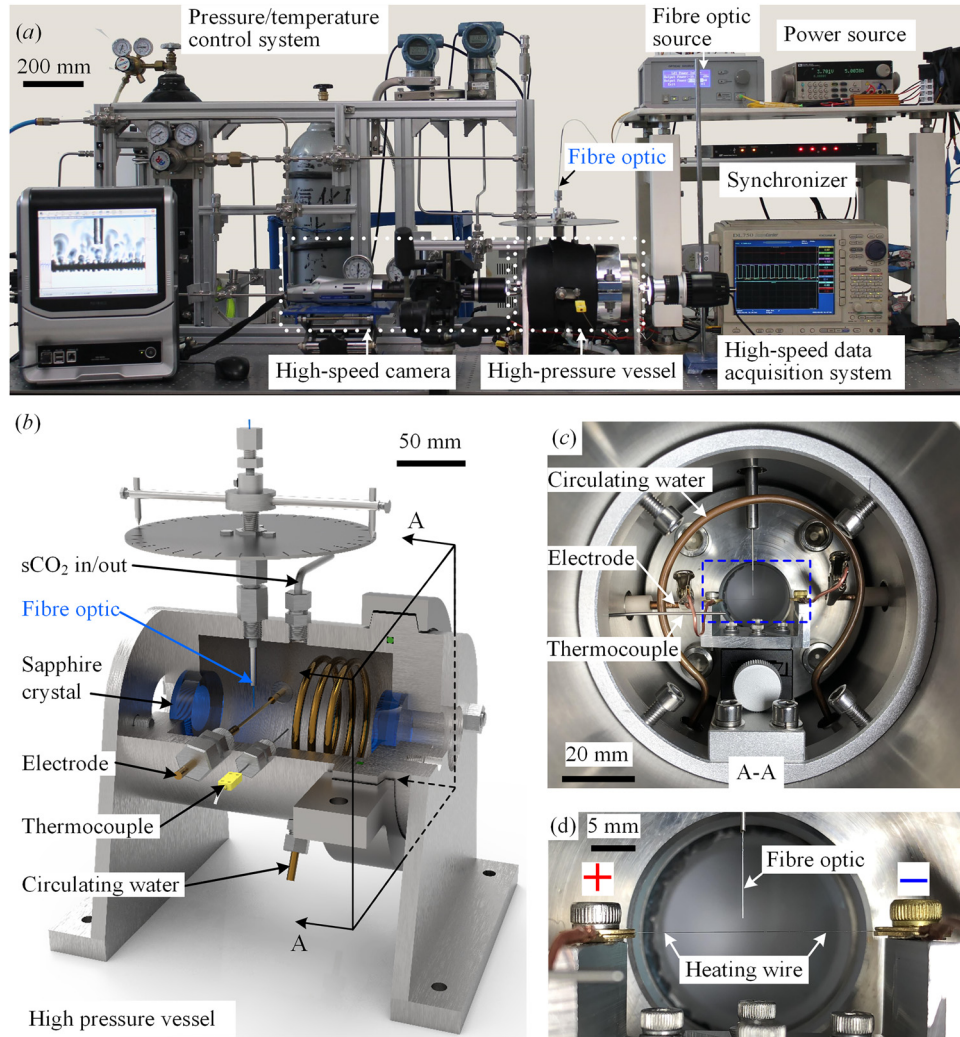
Fig. 4. Experiment setup. (a) photo of the experimental setup; (b) image focusing on the internal structure of high pressure vessel; (c) cross-section view of the high pressure vessel; (d) cross-sectional view focusing on the heater wire and the fibre optic.
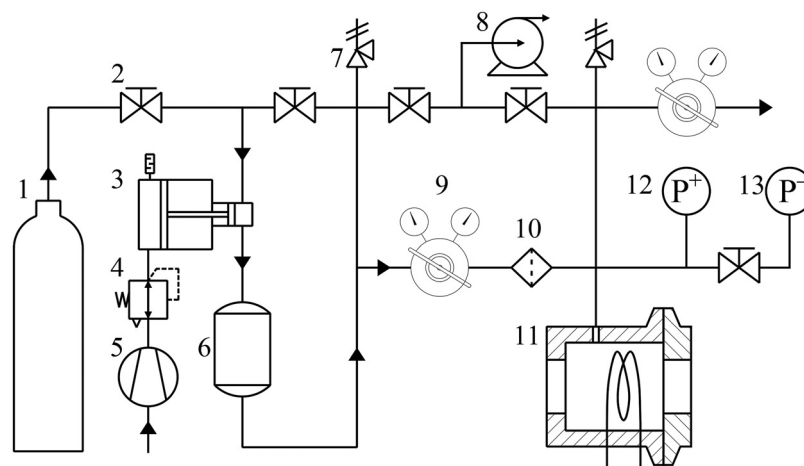
Fig. 5. The flow chart of the pressure control system (1. gas bottle containing high purity carbon dioxide; 2. cut-off valve; 3. piston pump; 4. filter regulator lubricator; 5. air compressor; 6. pressurized tank; 7. relief valve; 8. vacuum pump; 9. compression release valve; 10. filter; 11. high pressure vessel; 12. pressure transmitter; 13. vacuum transmitter.)
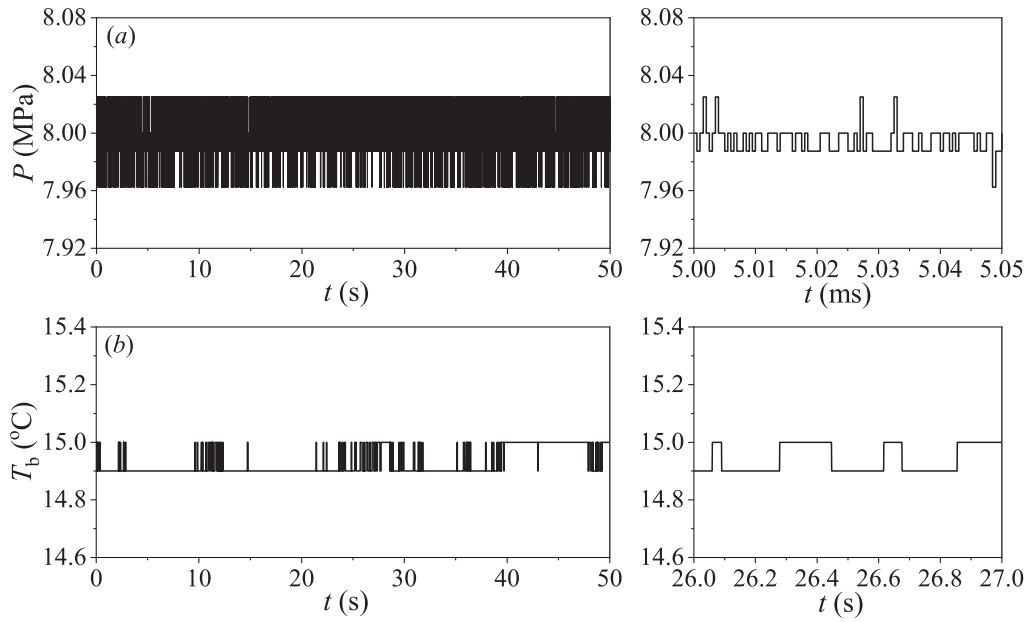
Fig. 6. The control outcome for the parameters of pressure and temperature (*a*) for pressure; (*b*) for temperature.
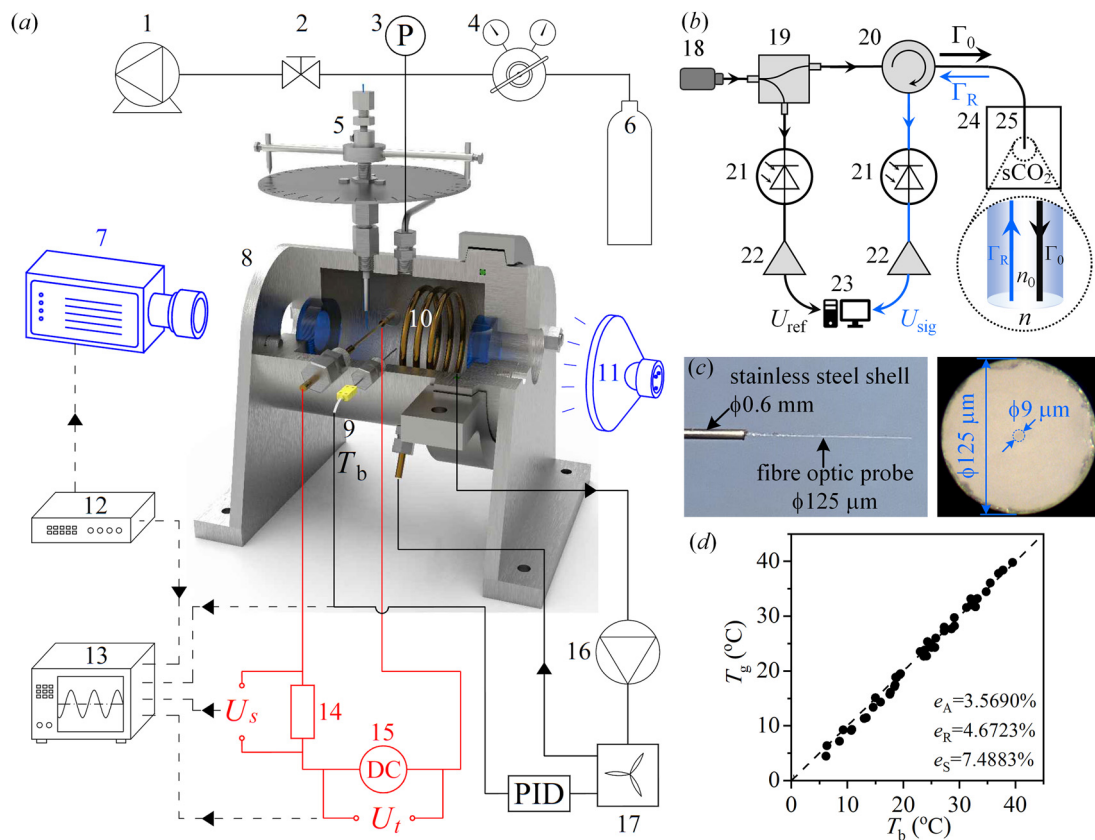

Fig. 7. Measurement system for heat transfer of Pt wire or NiCr wire in pool liquid of CO_2. (*a*) the whole system; (*b*) the electric circuit for the fibre optic measurement; (*c*) photo of the fibre optic; (*d*) calibration result of the temperature measurement by using fibre optic and precision thermocouple. (1. vacuum pump; 2. high pressure valve; 3. pressure transmitter; 4. compression release valve; 5. fibre optic adjustment facility; 6. high purity carbon dioxide tank; 7. high speed camera; 8. high pressure vessel; 9. thermocouple; 10. helical coiled tube to dissipate heat via the circulating water; 11. LED acting as the back light source; 12. synchronizer; 13. High speed data acquisition system; 14. reference resistance; 15. DC voltage generator; 16. circulating water pump; 17. water tank; 18. LED light; 19. splitter; 20. optic circulator; 21. photodiode; 22. amplifier; 23. data acquisition unit; 24. high-pressure vessel; 25. fibre optic probe.)

denoted as *sig* and *ref* respectively (see Fig. 7b). The signal beam passed through an optical circulator and entered the probe, where it was reflected from the end of the fibre. The intensities of the incident and reflected beams are Γ_0 and Γ_R, respectively. The reflected beam was returned to the optical circulator and deflected to the photodiode and amplifier, where it was converted into a voltage signal, U_{sig}. The reference beam from the splitter was directly converted into a voltage signal, U_{ref}, using another set of photodiode and amplifier. The ratio of Γ_R to Γ_0 is related to the refractive index of fluid n and is proportional to the ratio of U_{sig} to U_{ref} [36]:

$$\frac{\Gamma_R}{\Gamma_0} = \left(\frac{n - n_0}{n + n_0}\right)^2 = \kappa \frac{U_{sig}}{U_{ref}} \tag{8}$$

The refractive index of the silica fibres, n_0, is 1.45. The constant κ is related to the optical properties and losses along the light travelling path, but not to the fluid being measured. Therefore, κ should be calibrated in a fluid with a known refractive index, such as air. The ratio of the voltage in air, U_{sigair}/U_{refair}, satisfies the following condition:

$$\left(\frac{n_{air} - n_0}{n_{air} + n_0}\right)^2 = \kappa \frac{U_{sigair}}{U_{refair}} \tag{9}$$

Operating on Eqs. (8) and (9), κ is eliminated and n of the fluid is written as follows [36]:

$$n = n_0 \frac{\sqrt{\frac{U_{sigair}}{U_{refair}} \frac{U_{ref}}{U_{sig}}}(n_0 + n_{air}) - (n_0 - n_{air})}{\sqrt{\frac{U_{sigair}}{U_{refair}} \frac{U_{ref}}{U_{sig}}}(n_0 + n_{air}) + (n_0 - n_{air})} \tag{10}$$

At atmospheric pressure and room temperature of 20°C, the refractive index of air (n_{air}) is 1.00027. The Lorentz–Lorenz equation [36] gives the fluid density ρ as:

$$\rho = \frac{n^2 - 1}{A(n^2 + 2)} \tag{11}$$

For nonpolar molecules such as CO_2, A is a constant ($A=1.42\times10^{-4}$ m^3/kg), which is independent of temperature [36]. Once ρ is known using Eq. (11), the fluid temperature T_g can be determined based on the known relationship between ρ, T_g, and P in supercritical fluids.

Fig. 7c illustrates the fibre optic, which was prepared using a commercial communication fibre. Removing the plastic protective layer of the fibre left a fibre core and a reflective layer with diameters of 9 μm and 125 μm, respectively. The bare fibre was then inserted into a stainless-steel shell with a length and outer and inner diameters of 200 mm, 0.6 mm, and 0.4 mm, respectively. The sealant filled the gap between the fibre and shell. Because the 9 μm fibre core is one order of magnitude smaller than the 70 μm heater wire diameter, using the fibre measurement ensures high temporal and spatial resolutions.

After the system was assembled, careful calibration was performed for the fibre measurements. The calibration experiment was conducted in the pressure vessel with the ranges of pressures $P=(8\sim12)$ MPa and bulk fluid temperatures $T_b=(5\sim40)$°C. The fibre probe was placed close to a precision thermocouple at a distance of 30 mm. Fig. 7(d) shows the calibration outcome, in which T_g and T_b were measured using the fibre probe and the thermocouple, respectively. The results showed good agreement, with an average relative error e_A, an average square root error e_R, and an average standard deviation e_S of 3.57%, 4.67%, and 7.49%, respectively.

2.3.3. Characterisation of vapor–liquid interface

In subcritical pressures, a vapor–liquid interface has nanoscale thicknesses, inside and outside of which are vapor and liquid, respectively [37]. The bubble interface can be easily detected using

a high-speed camera because of the reflection of light at the interface. In contrast to the direct observation of bubbles at subcritical pressure, schlieren photography and shadowgraph methods are used to detect bubble-like structures in supercritical pressures [20–22]. These methods are density-sensitive techniques suitable for single-phase transparent fluids in shockwave and combustion applications [38,39]. Quantitative identification of bubble-like interfaces presents challenges when schlieren or shadowgraph techniques are employed for supercritical fluids. This is because the background light must pass through a series of lenses and mirrors before entering the camera, resulting in a loss of light intensity and image brightness.

Herein, we report a direct photography method for characterising the bubble-like interface in SF (see Fig. 8). Considering sCO$_2$ heated by a horizontally positioned Pt wire, the background LED light consecutively passes through the right optical window of the pressure vessel and the sCO$_2$ fluid in the pressure vessel and is collected by the camera via the left optical window of the pressure vessel. A practical density field over the cross-sectional wire is shown in Fig. 8(a), based on the calculation results of Yu et al. [40]. A low-density VL liquid exists near the wire, whereas a high-density liquid exists at a certain distance away from the wire. Fig. 8(b) shows the light travelling in a varied-density field within a circular radius r_0 assuming a point heat source at $z=0$. The fluid density ρ decreases towards the centre of the circle but is equal to the bulk value of ρ_b for $r>r_0$. Based on Eq. (11), the refractive index n, which is a function of r, is

$$n(r) = \sqrt{1 + \frac{3A}{\frac{1}{\rho(r)} - A}} \tag{12}$$

Eq. (12) indicates a decrease in $n(r)$ with a decrease in $\rho(r)$ in the circle; however, n equals to n_b for $r>r_0$. Assuming a horizontal light at z above the circle centre point O, we examine how the light is deformed while travelling in the circle. Recording α as the deflection angle, a light beam is more deflected from the camera lens with a larger α, under which the camera receives less light signal and forms a darker image. Based on the Fermat's principle, α can be written as [41]

$$\alpha = 2zn_b \int_{zu_b}^{u_b} \frac{d\ln n}{du} \cdot \frac{du}{[u^2 - z^2 n_b^2]^{1/2}} \tag{13}$$

A new variable $u=rn(r)$ is introduced, and $u_b=r_0 n(r_0)$. Hence, the function $n(r)$ is converted to $n(u)$, and u increases with an increase in r. The α can be numerically determined for any form of $n(u)$ using Eq. (13), but has an analytical solution using special forms of $n(u)$. Assuming $n(u)$ to be [41]

$$n(u) = \begin{cases} n_b e^{\left(\ln \frac{n_b}{n(0)}\right)\left[\left(\frac{u}{u_b}\right)^2 - 1\right]} & 0 \le u \le u_b \\ n_b u > u_b \end{cases} \tag{14}$$

Eq. (14) satisfies the decreased $n(u)$ towards the circle centre. The analytical solution for α is provided in [41].
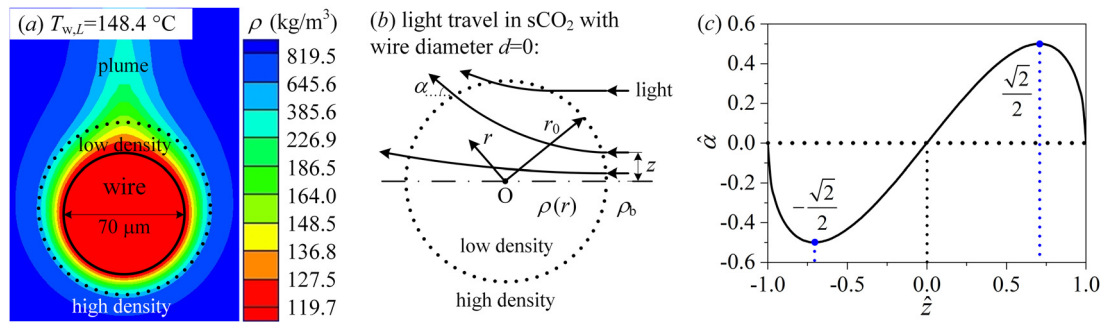
$$\alpha = \left(\frac{4}{r_0^2} \ln \frac{n_b}{n(0)}\right) \cdot z\sqrt{r_0^2 - z^2}, 0 \le z \le r_0 \tag{15}$$

Defining two non-dimensional parameters of $\hat{\alpha}$ and $\hat{z}$, Eq. (15) becomes

$$\hat{\alpha} = \frac{\alpha}{4 \ln \frac{n_b}{n(0)}}, \hat{z} = \frac{z}{r_0}, \hat{\alpha} = \hat{z}\sqrt{1 - \hat{z}^2} \text{ with } -1 \le \hat{z} \le 1 \tag{16}$$

Eq. (16c) expresses the curves shown in Fig. 8(c). The curve indicates three $\alpha=0$ points at $z=-r_0$, $z=0$, and $z=r_0$, implying straight light transmission without loss of light intensity at these

Fig. 8. Light transmission in varied density field for NiCr wire heater. (a) the calculated density field with P=8 MPa, q=261 kW/m^2 and T_b=15°C; (b) schematic diagram of light path assuming wire diameter d=0; (c) variation of dimensionless deflection angle $\hat{\alpha}$ with dimensionless coordinate $\hat{z}$.

three locations. The loss of light intensity is maximized at $z = -\sqrt{2}r_0/2$ and $z = \sqrt{2}r_0/2$. The results indicate that the light deformation depends on the direction of the light path and the fluid density gradient. If the light transmission direction is consistent with the direction of the fluid density variation, the light remains straight without a loss of intensity. However, if the light path is perpendicular to the direction of fluid density variation, the light deformation occurs with a loss of light intensity. This conclusion helps to understand the brightness/darkness pattern observed in supercritical fluids.

The images captured by the high-speed camera shows an increase in heat flux (see Fig. 9). The wire was enclosed by a vapor layer. Owing to the density variation in the height direction, a plume structure formed above the wire. The vapor layer and the plume were stable at a lower heat flux (see Fig. 9a). For a location sufficiently high above the wire, a weak deformation of the light occurred, yielding a brighter image owing to the smaller density gradient at point A. If the point was close to the wire, strong deformation occurs, yielding a darker image owing to the significant density gradient at point B. As shown in Fig. 9(b), when the heat flux increased, the plume above the wire became unstable. An obvious fluid-density gradient occurred in the height direction, even though point C was far from the wire. Because the light direction was not consistent with the fluid density variation direction, strong deformation occurred at point C. This explained the two dark regions shown in Fig. 9(b), with one dark region enclosing the wire, and the other darker region above the wire, forming an alternating dark/bright/dark pattern. When the heat flux increased, as shown in Fig. 9(c), in addition to the VL film enclosing the wire and the unstable plume above the wire, bubble-like structures were observed under the wire. We compare the light paths emitted from two points D and E, in which D is closer to the wire centre than E. Based on Fig. 8(c), D and E correspond to the formation of a brighter dot image owing to its proximity to the wire centre and a darker dot image owing to its further distance from the wire centre (but not reaching the edge of the bubble-like structure).

Next, we characterize the vapor–liquid interface during pseudo-boiling. The thickness δ of the VL layer is an important parameter. The photograph in Fig. 10(a) depicts a wire submerged in sCO$_2$ at room temperature and approximately 8 MPa, where the diameter of the pure black region is exactly equal to the wire diameter. At q_L=495.4 kW/m^2, three kinds of structures were observed: an upward plume, a VL layer, and bubble-like structures. Two baselines can be marked for VL, the diameter of which is D. Hence, the VL thickness is $\delta = (D - d)/2$ (Fig. 10b).

In subcritical pressures, the location of the bubble interface was independent of the light power used to capture the image. However, the fluid density has gradual variations in supercritical pressures, resulting in a bubble-like interface that is dependent on the light power used to capture the image. At a constant condition of

P=8 MPa, q_L =436.5 kW/m^2 and T_b=15°C, Fig. 11(a) displays a sequence of images captured at six different light powers (LP) ranging from 3 W to 32 W. When the LP is raised, the black regions in the images become narrower, as demonstrated in the six images.

The vapor–liquid interface was obtained using the MATLAB software based on image files captured by a high-speed camera. An image file can be converted into a 640×480 matrix, with each element in the matrix representing a grey value recorded as C, covering a range of (0–255), with 0 and 255 representing pure black and pure white, respectively. The non-dimensional grey is defined as

$$\hat{C} = \frac{C - C_{\min}}{C_{\max} - C_{\min}} \tag{17}$$

where $C_{\max}$ and $C_{\min}$ are the maximum and minimum grey values of each image, respectively, where $\hat{C} = 0$ and $\hat{C} = 1$ represent the light completely shadowed by the wire and the brightest point, respectively. Fig. 11(b) shows plots of $\hat{C}$ versus z in the height direction. The baseline of the VL layer is marked at $\hat{C} = 1$; therefore, the thickness δ is 95.2 μm, 57.2 μm and 43.9 μm with the light powers of 5 W, 10 W, and 20 W, respectively. The δ decreases with an increase in light power, as shown in Fig. 11(c). Saturation δ is achieved beyond which δ does not decrease. The transition from decrease to saturation takes place at $LP \approx$20 W; hence, the data with LP=20 W are used for the following analysis. Previously, the vapor–liquid interface was assumed to occur at the pseudo-critical temperature T_{pc} [42]. Instead, the grey capture method is used to locate the interface in this study. Each point in the image has a specific temperature that can determine the fluid density at that point [40]. Fig. 11(c) also plots the density at the interface ρ_{IF}, indicating $\rho_{IF} < \rho_{pc}$ at LP>10 W. This observation implies that the grey capture method has a thinner vapor layer than that determined by the pseudo-critical point assumption.

2.4. Uncertainties of various parameters

The signals of U_s, U_t and T_b were recorded by a high-speed data acquisition system (Yokogawa DL750, Japan) at a recording rate of 4000 Hz, which was sufficient to capture the dynamic process during pseudo-boiling. The voltage measurements had an uncertainty of 0.5%. T_b had an uncertainty of 0.2°C. T_g was measured by the fibre optic, having the average errors e_A, e_R and e_S of 3.57%, 4.67%, and 7.49% respectively, when compared with those of the precise thermocouple measurements. T_g had a response time of microseconds, which was at least two orders of magnitude faster than that of thermocouples. P was measured using a Rosemount 3051 pressure transducer with a response time of approximately 10 ms and an uncertainty of 0.075%. Driven by the LED light source, a high-speed camera (Keyence VW-9000, Japan) captured the pseudo-boiling process at a recording rate of 4000 fps, focusing on an area
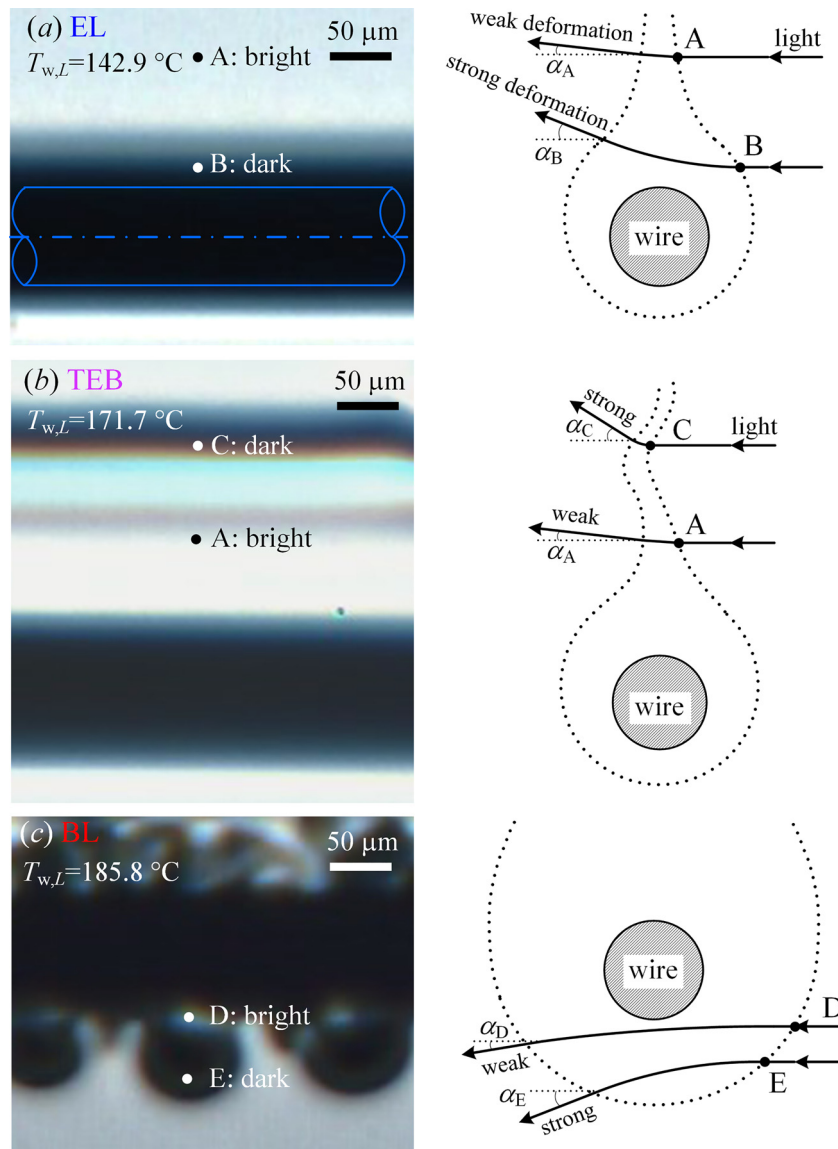
Fig. 9. Images taken by high speed camera and light transmission principle with $P=8$ MPa and $T_b=15$ °C for (*a*) $q_L=271.2$ kW/m², (*b*) $q_L=351.1$ kW/m² and (*c*) $q_L=451.9$ kW/m², respectively.

of 640 ×480 pixels for each image with a resolution of 1.9 μm. A synchroniser (MotionPro Timing Hub, IDT, USA) coordinated the high-speed camera, the high-speed data acquisition system, and the fibre optic measurement system, with a synchronising error of 20 ns for different systems. Experiments were performed at pressures of 8 MPa and 10 MPa, which were higher than the critical pressure of 7.377 MPa for CO_2. The two pressures were well controlled to be within 7.955~8.048 MPa and 9.928~10.035 MPa. The bulk CO_2 temperature was well controlled to be in the 5~50°C range, but only the data with $T_b=15$°C were used in this study. The heat flux at the wire surface q_L covered a wide range of 0~1822.0 kW/m². The maximum wire temperatures $T_{w,L}$ could reach 883.1°C. The errors of q_L and h_L could be obtained using the error transmission principle [43], and were 1.74% for q_L and 4.84% for h_L. Table 2 summarized the ranges, uncertainties, and response times for various parameters.

## 3. Pseudo-boiling with the Pt wire

The boiling curves of $h_L \sim \Delta T_{w,L}$ and $q_L \sim \Delta T_{w,L}$ are plotted in Fig. 12 for the Pt wire, where $\Delta T_{w,L} = T_{w,L} - T_{pc}$ is the wall su-

Table 2
Parameter measurements and uncertainties.

Parameter	Range	Error	Response time
pressure P	7.955~10.035 MPa	0.075%	<100 ms
pool liquid temperature T_b	14.9~15.1°C	0.1°C	<250 ms
voltage U	0~19 V	0.5%	<1 μs
wire temperature $T_{w,L}$	15~850°C	3.71%	<1 μs
heat flux density q_L	0~1822.0 kW/m²	1.74%	<1 μs
heat transfer coefficient h_L	0~4703.8 kW/m²K	4.84%	<1 μs
fibre optic temperature T_g	15~40°C	3.57%	<10 μs
VL film sickness δ	0~78.1 μm	1.9 μm	<250 μs

perheating and T_{pc} is the pseudo-critical temperature. The natural convection (NC) and the EL mode are observed, representing single-phase convection and pseudo-boiling, respectively. The two regions of heat transfer interface at the peak heat transfer coefficient. Fig. 13 presents the images at various heat fluxes and the quasi-stable wall temperatures versus time. In the NC region, h_L sharply increases with an increase in wall superheating or heat flux. The NC is dominated by the Grashof number, which is defined
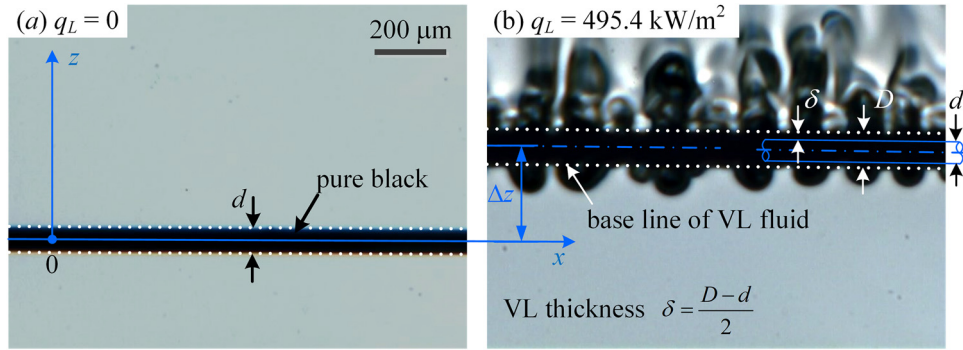
Fig. 10. Definition of the VL film thickness δ and wire displacement Δz. (a) Width of the purely black area equals to the wire diameter d before heating. (b) The pure black area expands to D after heating.
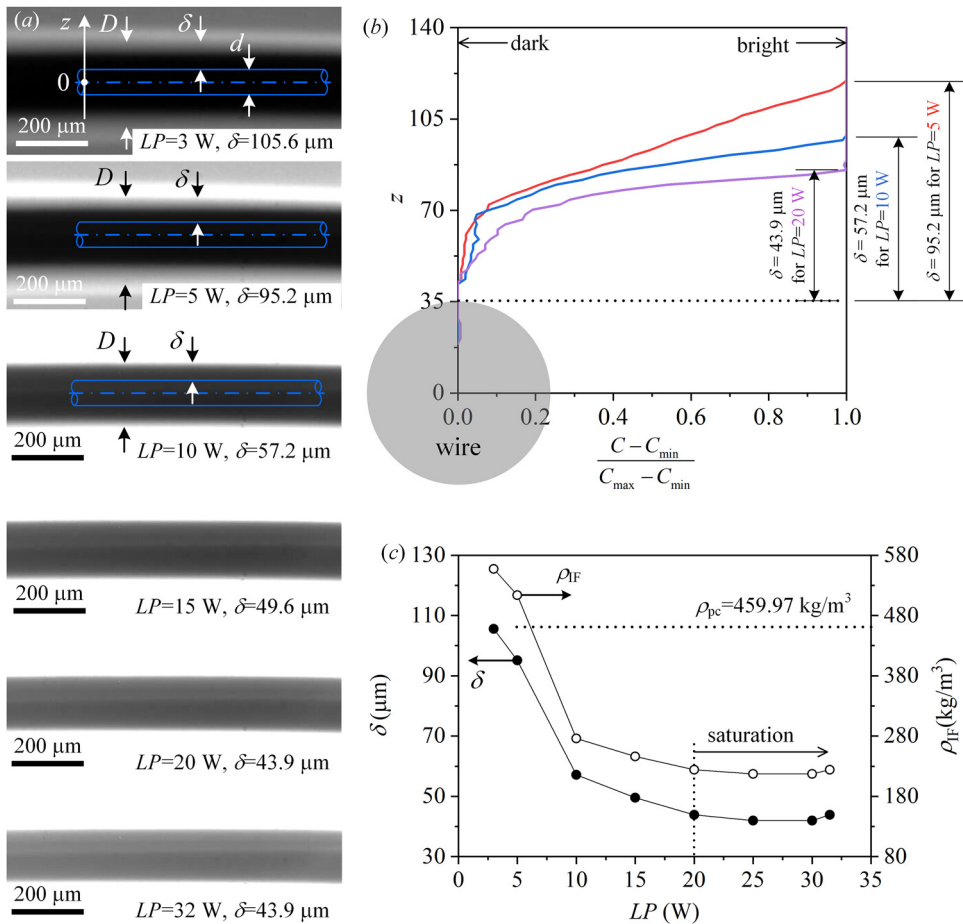
Fig. 11. VL film sickness δ at different light power LP for Pt wire heater with $P=8$ MPa, $q_L=436.5$ kW/m² and $T_b=15$°C. (a) images showing the decreased δ with increase of LP; (b) dimensionless grey level C/C_{max} of images to determine the vapor-liquid interface; (c) the determination of δ and ρ at the vapor-liquid interface at different LP.

as [44]

$$Gr = \frac{g\beta \Delta T_{w,L} d^3}{\nu^2} \tag{18}$$

where g is the gravitational acceleration, β is the expansion coefficient per unit of K, d is the characteristic length, which is the wire diameter for the present problem, and ν is the dynamic viscosity.

In the framework of single-phase heat transfer, a larger wall superheating results in a larger buoyancy force to overcome the viscous force to enhance heat transfer, explaining the increase in h_L or q_L with increases in $\Delta T_{w,L}$. The increase trend stops at $\Delta T_{w,L}=17.3$°C at 8 MPa and 22.3°C at 10 MPa. Because the wire temperature exceeds the pseudo-critical temperature, VL layer

forms in the NC region, as shown in the image with $\delta=6.4$ μm at $q=69.5$ kW/m² in Fig. 13(a). Compared with the NC in subcritical pressures, the NC in supercritical pressures is dominated by the buoyancy effect and VL layer effect; the former enhances heat transfer, but the latter deteriorates heat transfer. Hence, heat transfer cannot be further enhanced beyond the maximum point of h_L.

In the EL region, h_L gets a quicker decrease and then varies slightly with wall superheating. The increasing VL layer thickness δ increases the thermal conductivity resistance of the layer, which explains the decayed heat transfer in the EL region (see Fig. 13b). In contrast to the continuous decrease of h_L, a recovery trend of h_L is observed at high wall superheating such as >287°C. Yu et al. [40] explained the recovered heat transfer at high-wall superheat-
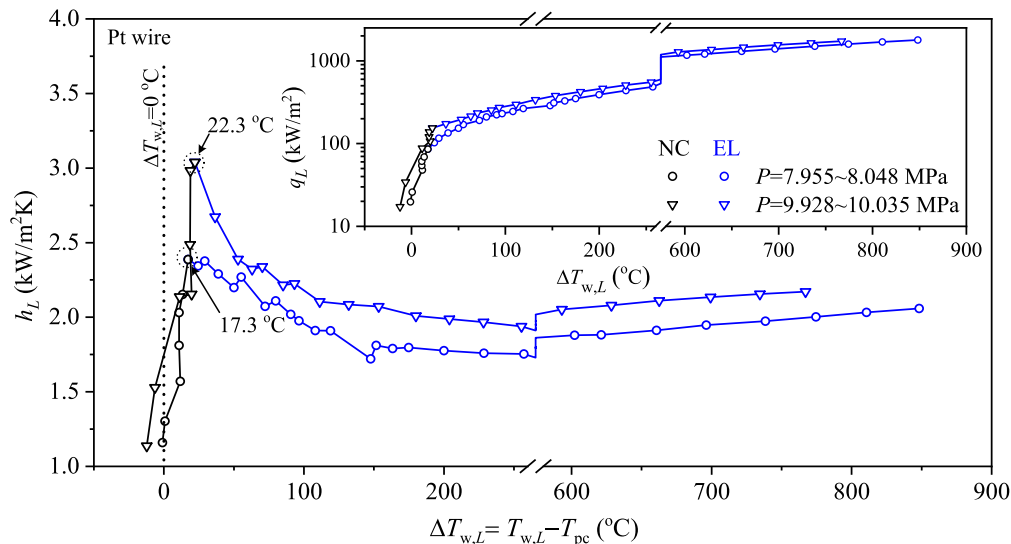
Fig. 12. Heat transfer coefficients h_L dependent on wall superheating $\Delta T_{w,L} = T_{w,L} - T_{pc}$ for the Pt wire with P=8 and 10 MPa, T_b=15°C, noting that the insert figure shows the boiling curve corresponding to the main figure.
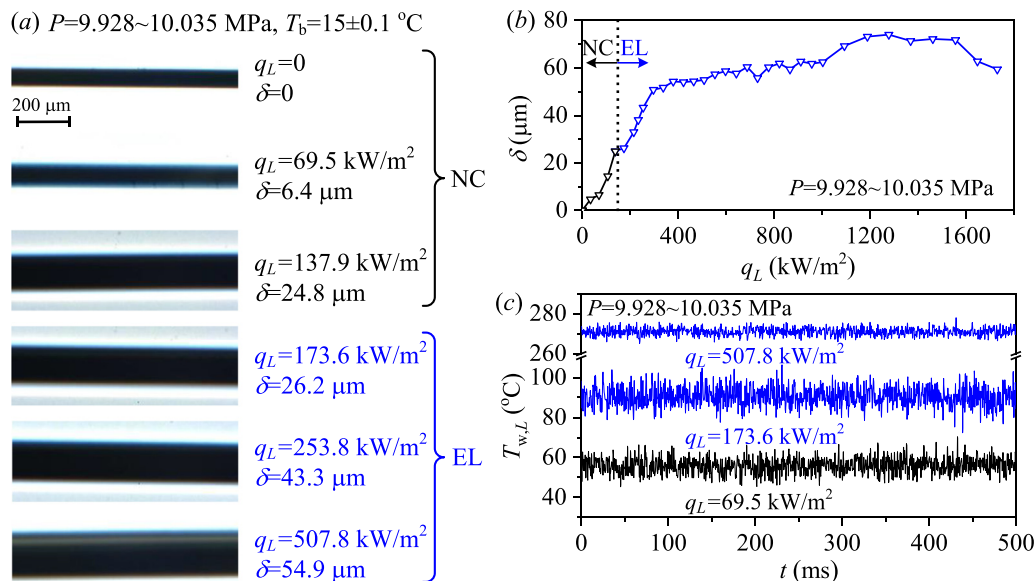
Fig. 13. Characteristics of NC and EL heat transfer for the Pt wire with P=10 MPa and T_b=15 °C. (*a*) images taken in NC and EL regions; (*b*) variation of δ with heat flux q_L; (*c*) quasi-stable wall temperature $T_{w,L}$ in NC and EL regions.

ing with the increased thermal conductivity of the supercritical fluid. Even though the VL layer is thicker at high wall superheating, the increase in the thermal conductivity of the fluid causes a slight increase in the heat transfer coefficients. Furthermore, minor variations in the wire temperatures can be observed in Fig. 13(*c*) in both NC and EL regions, indicating a relatively stable heat transfer process (see Supplementary Movies 1 and 2).

Effect of pressures on heat transfer is discussed here. The outcomes shown in Figs. 12 and 13 correspond to two pressure levels of 8 MPa and 10 MPa, respectively. Although the curves of $q_L \sim \Delta T_{w,L}$ show weak changes at the two pressures, the heat transfer coefficients are significantly larger at 10 MPa than those at 8 MPa. Zhu et al. [45] proposed the supercritical boiling number (*SBO*) to characterise the convective heat transfer of sCO$_2$ in tubes. The *SBO* represents the competition between evaporation momentum force and inertia force, in which the former adheres the VL layer on the wall to deteriorate heat transfer, but the latter makes the VL layer thinner to enhance heat transfer. The increase of pressure increases

the enthalpy at the pseudo-critical point to decrease the VL layer thickness, explaining the improved heat transfer with the increasing pressure. This conclusion is also applicable for pool BL heat transfer in supercritical pressures.

4. Pseudo-boiling with the NiCr wire

4.1. Natural convection and evaporation-like mode

In contrast to the Pt wire, the NiCr wire demonstrates four regions of heat transfer: NC region, EL region, TEB region, and BL region. The boiling curves at 8 and 10 MPa are shown in Fig. 14(*a*), (*b*), and (*c*). The NC region is narrow, with a steep increase in the heat transfer coefficients versus wall superheating. Then, the heat transfer coefficients decrease in the EL region, followed by a significant recovery or enhancement in heat transfer, accompanied by heat transfer oscillations in the TEB and BL regions. The VL layer thicknesses are shown in Fig. 14(*d*), with heat fluxes varying from
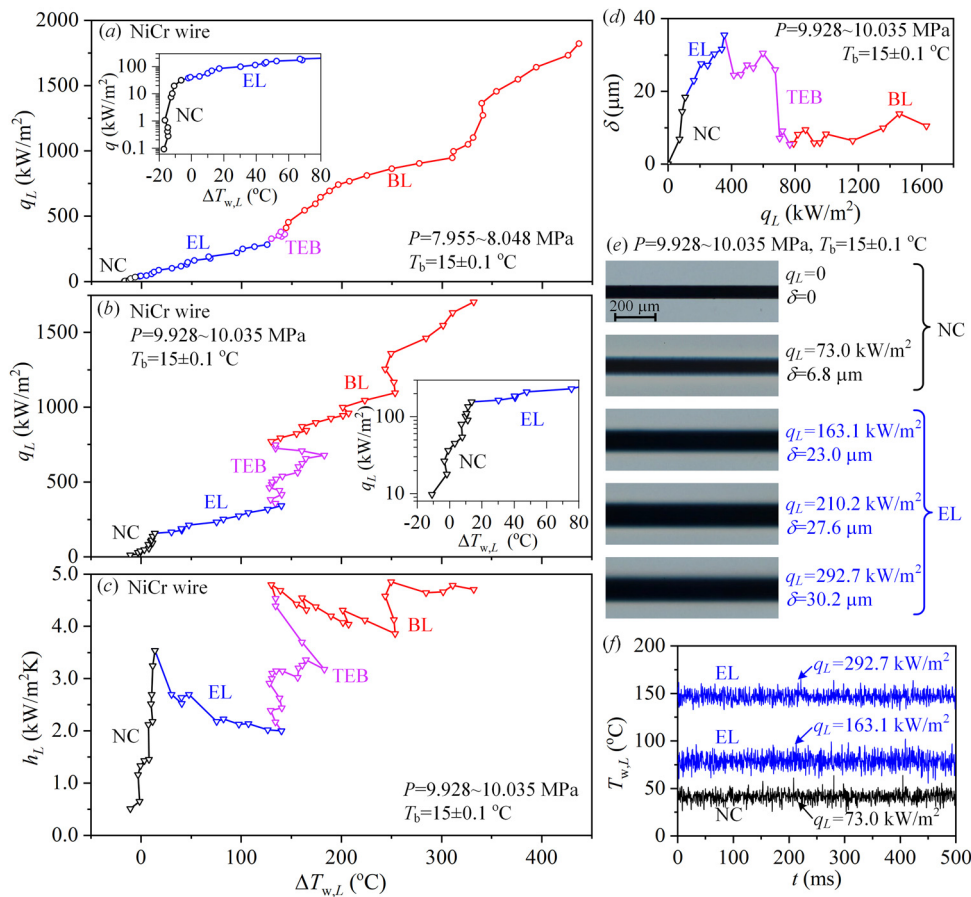
Fig. 14. Heat transfer characteristics of the NiCr wire with P=8 and 10 MPa and T_b=15 °C. (*a*) boiling curve at 8 MPa; (*b*) boiling curve at 10 MPa; (*c*) heat transfer coefficients h_L dependent on wall superheating $\Delta T_{w,L}$ at 10 MPa; (*d*) VL layer thickness δ versus q_L at 10 MPa; (*e*) images taken in NC region and EL region at 10 MPa; (*f*) quasi-stable wall temperatures in NC region and EL region.

0 to 1632.8 kW/m². In the NC and EL regions, δ exhibits a sharp increase with an increase in q_L (see Fig. 14*d* and *e*), which is similar to that of the Pt wire. The temperature of the NiCr wire is quasi-stable over time in the EL region (Fig. 14*f*). The dynamic processes of NC and EL regions on the NiCr wire are shown in Supplementary Movies 3 and 4, respectively.

4.2. Transition from evaporation-like to boiling-like mode

Here we focus on the TEB region. A typical case with q_L=402.6 kW/m² at 10 MPa is shown in Fig. 15(*a*), with the wire temperature oscillating in the (128.9∼168.8°C) range. Note that the fibre optic is 200 μm above the wire, the fibre optic sensitively detects the temperature variations in the local flow field, with T_g oscillating in the 16.4∼40.8°C range. Although the total voltage applied to the standard resistance and the wire keeps constant, the electric current is changing owing to the temperature dependent electric resistance of the wire, explaining the mini variations of heat fluxes in a narrow range of (401.9∼403.6) kW/m². Furthermore, the heat transfer coefficients oscillate in the (2.6∼3.5) kW/m²K range (see Fig. 15*b*). The fast Fourier transform yields a dominant frequency of 3.86 Hz for $T_{w,L}$ and T_g (Fig. 15*c* and *d*), corresponding to an oscillation period of 259 ms for $T_{w,L}$, T_g, q_L, and h_L. An oscillating cycle includes an EL stage, represented by blue, and a BL stage, represented by red (see Fig. 15*a* and *b*). A lower wire temperature and a higher heat transfer coefficient imply improved heat transfer in the BL stage than in the EL stage.

To understand the periodic heat transfer in the TEB region, the dynamic motion of the wire is shown in Fig. 16 and Supplemen-

tary Movie 5. The EL stage keeps a flat VL layer thickness in the 26.6∼29.5 μm range, but the BL stage reduces δ to a minimum value of 3.8 μm. The fast Fourier transform gets two dominant frequencies of 3.86 Hz and 103.64 Hz, with the former corresponding to the cycle period and the latter representing the characteristic frequency of bubble-like pattern (see Fig. 16*a* and *b*). The oscillation of the wire displacementΔzconfirms the piston motion of the wire, where$\Delta z$is the instantaneous wire location relative to the balanced location of the wire in the height direction. Initially, in the cold state, the wire was straight, with the wire centre located at z=0. Owing to the line-expansion effect, an increase in the wire temperature elongates and deforms the wire. In the EL stage, the positive and increased displacements indicate the upward motion of the wire, during which a VL film encloses the wire. In the BL stage, the decreased displacement indicates a downward motion of the wire, during which not only the VL layer encloses the wire, but also a bubble-like layer occurs underneath the wire (see Fig. 16*c*). In the BL stage, the enhanced heat transfer was caused by the faster motion of the wire and the bubble-like phenomenon.

In subcritical pressures, bubbles nucleate, grow, and depart more easily on the upward-facing surface than on the downward-facing surface [46]. However, this does not hold in supercritical pressures, where bubble-like structures occur below the wire. Fig. 17 shows the wire temperatures at different points marked in the curve. Fig. 18 tracks the lifetime of a bubble-like structure across EL and BL stages by marking different points from 1 to 8. The wire temperatures and images are shown in Fig. 17 and 18(*a*), respectively. Fig. 18(*b*) shows the tracking of the vapor–liquid interface during its lifetime. Quasi-flat interfaces are observed from
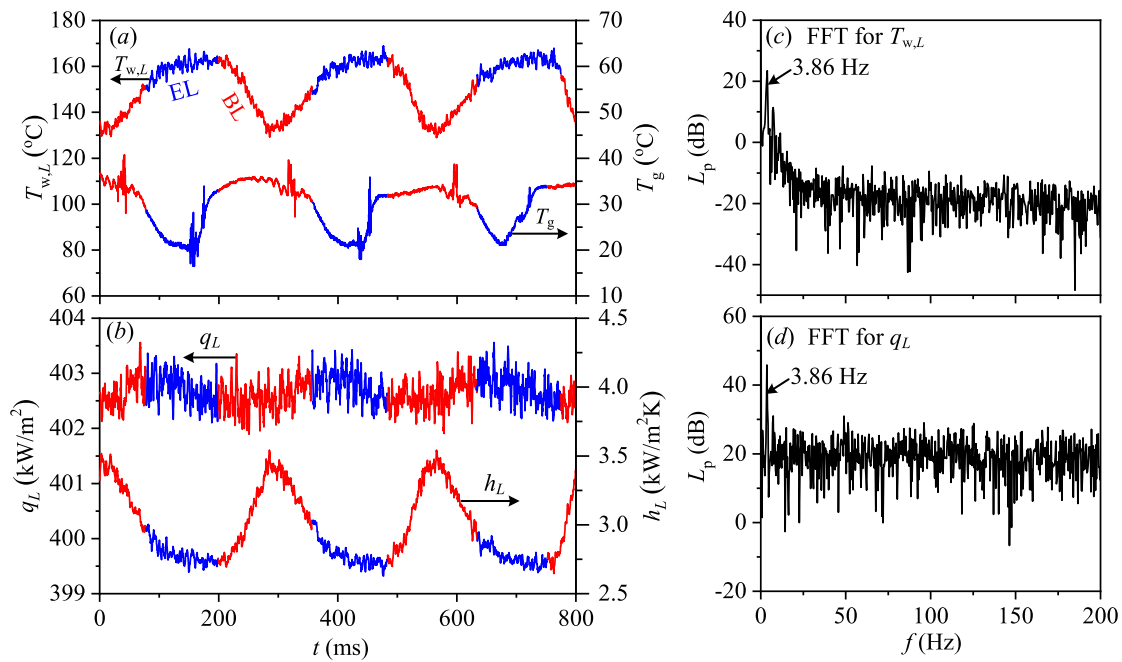
Fig. 15. Oscillating heat transfer for the NiCr wire in the transition region TEB with P=10 MPa, q_L=402.6 kW/m^2 and T_b=15 °C. (a) varied $T_{w,L}$ and T_g against time; (b) varied q_L and h_L against time; (c) frequency analysis of $T_{w,L}$ signal; (d) frequency analysis of q_L.
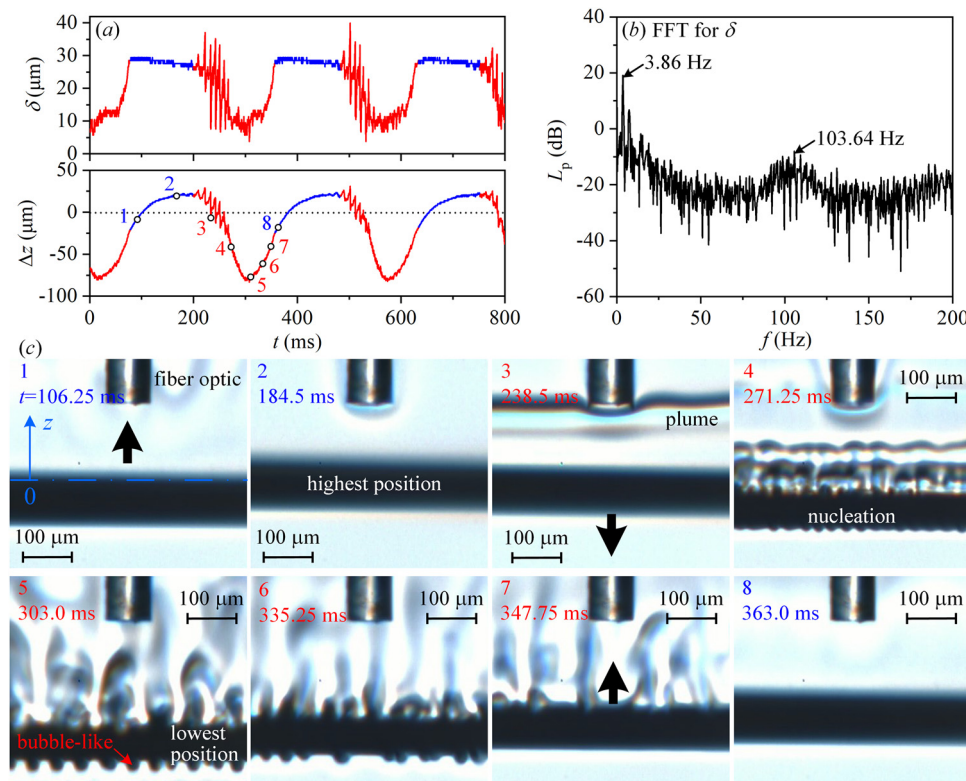
Fig. 16. Dynamic heat transfer in the TEB region for the NiCr wire with P=10 MPa, q_L=402.6 kW/m^2 and T_b=15°C. (a) variations of VL layer thickness δ and wire displacement Δz versus time; (b) frequency analysis of δ; (c) piston motion of the NiCr wire, noting EL heat transfer during upward moving of the wire, and BL heat transfer during downward moving of the wire.

102.5 ms to 162.5 ms in the EL stage. The BL stage consists of two substages: bubble-like nucleation/growth and collapse. Bubble-like nucleation is triggered by a transition from a flat interface to a curved one, which is different from bubble nucleation in micro-cavities on the wall at subcritical pressures. When the bubble-like

pattern reaches its maximum size at 182.75 ms, it again contracts to achieve a flat interface.

The expansion and contraction of bubbles in tens of milliseconds disturb the local flow field, enhancing the heat transfer between the bubble-like structure and the bulk liquid and explaining
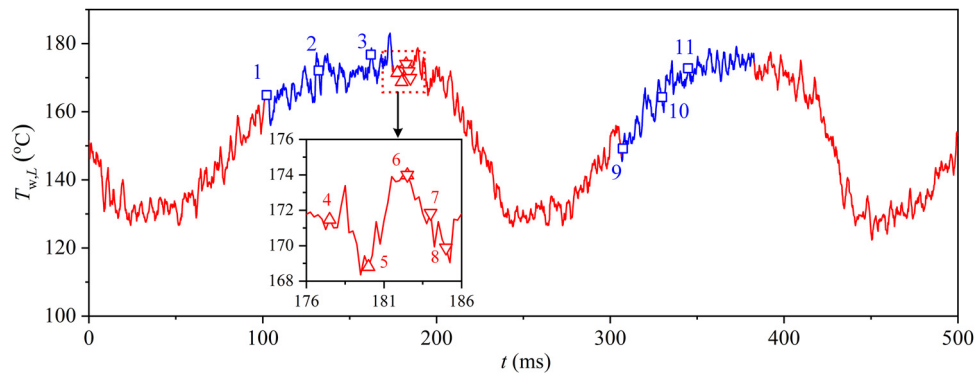
Fig. 17. Fluctuations of $T_{w,L}$ in which different points are marked in the TEB region for the NiCr wire with P=8 MPa, q_L=326.1 kW/m^2 and T_b=15°C.
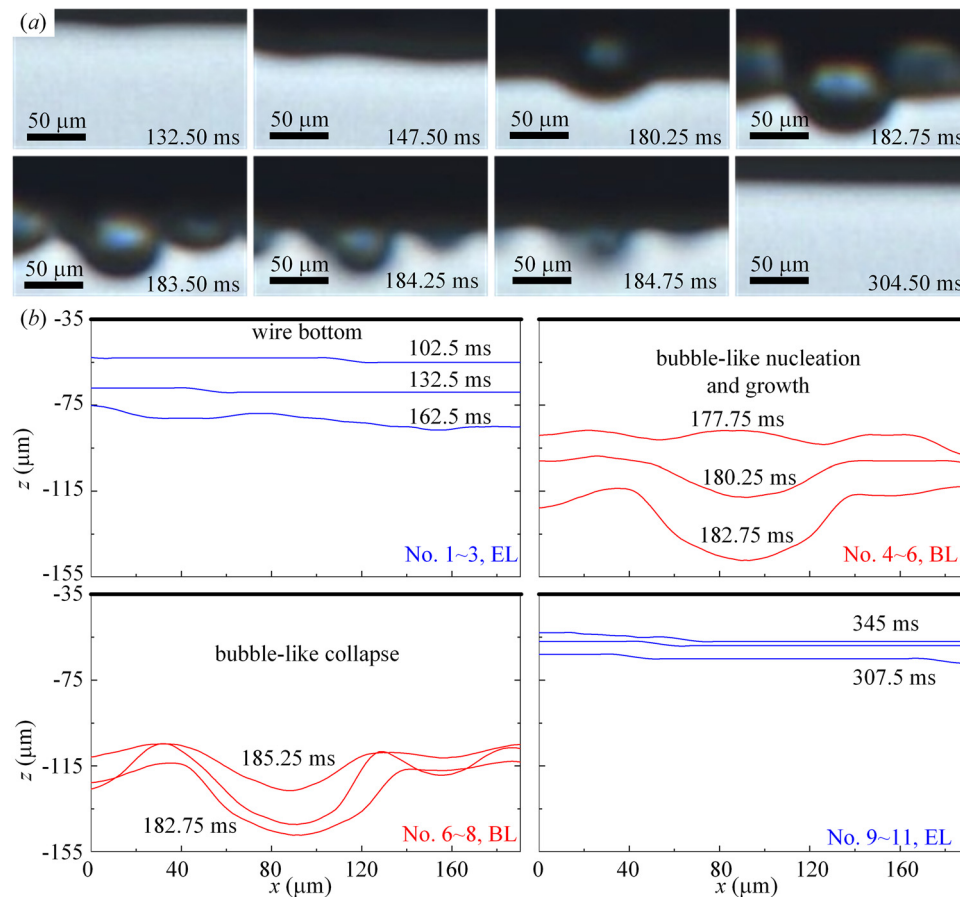

Fig. 18. Quantitative characterization of the vapor-liquid interface in the TEB region for the NiCr wire with P=8 MPa, q_L=326.1 kW/m^2 and T_b=15°C. (*a*) tracking images showing nucleation, growth and collapse of a bubble-like pattern; (*b*) quantitative tracking of the bubble-like interface.

the improved heat transfer in the BL stage compared to that in the EL stage. This dynamic is similar to subcooled boiling in subcritical pressures, in which bubbles can be completely condensed before they depart from the wall; however, it is different from saturation boiling, where the bubbles depart from the wall [47]. The simulation of supercritical heat transfer in a single-phase fluid framework has a long history [48,49]. Recently, pseudo-boiling was simulated based on a multiphase flow framework, in which the volume of fluid (VOF) technique, which is widely applied in subcritical pressures, was suggested to capture the vapor–liquid interface under supercritical pressures [42]. To the best of our knowledge, this is the first experimental demonstration of bubble-like dynamics and could serve as a benchmark for future comparisons with simulation results.

4.3. Boiling-like mode with the NiCr wire

With an increase in the heat flux beyond the TEB region, the EL substage disappears, resulting in a complete BL mode. The bubble-like dynamics in the BL region are similar to those in the BL substage in the TEB region. At subcritical pressures, boiling exhibits random, disordered, and chaotic characteristics [50]. The BL behaviour at supercritical pressure is shown in Fig. 19 and Supplementary Movie 6. High frequency/small amplitude oscillations occur for $T_{w,L}$, T_g, q_L, h_L, δ, andΔz, whose peak-to-peak value (defined as maximum subtracting minimum) are 29.3 K, 16.3 K, 5.1 kW/m^2, 0.5 kW/m^{2}K, 14.3 μm, and 21.0 μm, respectively, for the six signals. A positive displacement indicates that the wire is above the balance position z=0, which will be explained later by the
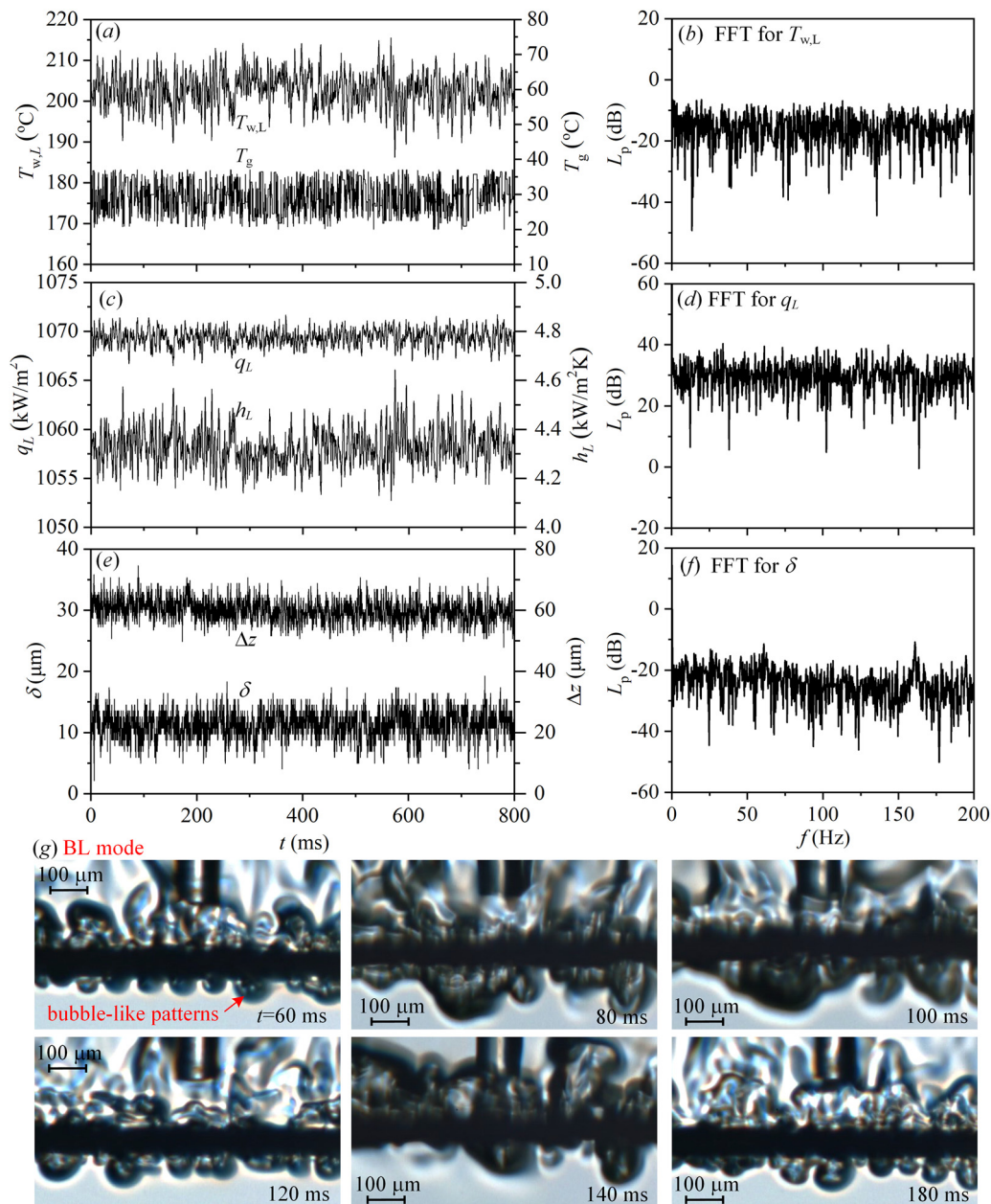
Fig. 19. High frequency oscillations of heat transfer in the BL region for the NiCr wire with $P=10$ MPa, $q_L=1069.3$ kW/m^2 and $T_b=15$°C. (a) oscillations of $T_{w,L}$; (b) frequency analysis for $T_{w,L}$; (c) oscillations of q_L; (d) frequency analysis for q_L; (e) oscillations of δ; (f) frequency analysis for δ; (g) bubble-like pattern.

force analysis. The fluid-solid coupling generates a piston motion of the wire with a small amplitude; in turn, the piston motion enhances heat transfer. The fast Fourier transform yields no dominant frequency, implying random and disordered characteristics of the BL mode.

Evaporation and boiling are two heat transfer modes under subcritical pressures. Only the EL mode occurs with the Pt wire, whereas both the EL and BL modes occur with the NiCr wire. The similarities and differences of boiling at subcritical and supercritical pressures are discussed. In subcritical pressure, assuming pure liquid without non-condensable gas and solid particles, a very high liquid temperature such as $(0.91\sim0.93)T_c$, where T_c is the critical temperature, is required to create a bubble embryo, which is called the homogeneous nucleation [51]. Depending on the wall wettability and microcavities, boiling can occur on the wall; this is called the heterogeneous nucleation (Fig. 20a). The nucleation theory as-

sumes that the energy in liquid molecules is distributed such that only a small portion is significantly larger than the average [52]. The activation energy is assumed to initiate the process of producing a vapor embryo. Nucleation is assumed to occur via a stepwise collision process [52].

Bubble nucleation and growth significantly alter the flow and temperature fields near the wall. The following three mechanisms govern the heat transfer process (see Fig. 20a): (I) transient conduction (TC): During a bubble departing from a heater surface, it is replaced by the bulk liquid. Heat is transferred by the TC to the liquid, enhancing heat transfer with higher bubble frequencies and smaller bubble sizes [53]. (II) Micro-convection: The rapid movement of the bubble interface causes liquid motion. Microconvection at the bubble interface contributes to the heat transfer enhancement as the interface velocity increases [54]. (III) Microlayer evaporation: This mechanism results from the evaporation of
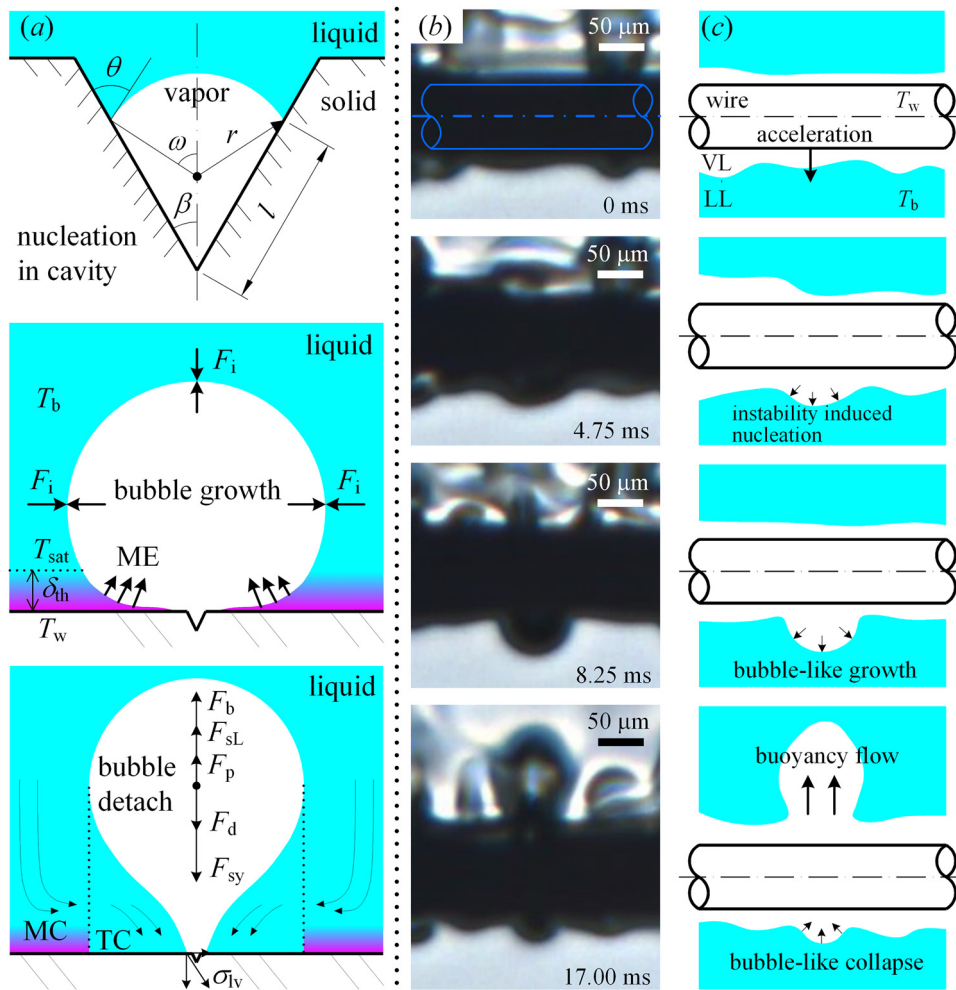
Fig. 20. bubble dynamics in subcritical pressure and supercritical pressure. (*a*) bubble nucleation, growth and departure for boiling in subcritical pressure based on Cole [52], where θ is the contact angle, β is the half conical angle, ω is the half angle of the bubble ball crown and l is contact length of the bubble embryo on the side surface of the conical cavity; (*b*) images taken for bubble-like nucleation, growth and collapse for the NiCr wire with $P=10$ MPa, $q_L=326.1$ kW/m^2 and $T_b=15°$C; (*c*) replotting of bubble-like dynamics based on (b).

a thin liquid layer underneath a bubble with a small contribution to heat transfer, even when the heat flux increases [54].

The bubble departure size is a key parameter that influences the heat transfer. Bubble growth involves inertia and thermal-dominated stages [37]. Various forces are applied to the bubble to determine its departure size (Fig. 20*a*). Drag force F_d and surface tension force F_{sy} tend to adhere the bubbles on the heater surface; however, the buoyancy force F_b, shear force F_{sL} and contact pressure force F_p are the driving forces for bubble detachment [55]. Once a net-zero force is reached, the bubble tends to detach. For a given heat flux, smaller departure diameters correspond to higher bubble frequencies, which are beneficial for heat transfer. A detailed comment on bubble dynamics under subcritical pressures is beyond the scope of this study. The present study draws attention to the BL characteristic at supercritical pressures.

Bubble-like nucleation: A bubble-like embryo is formed on a VL layer under supercritical pressure (Figs. 16–20). The piston motion of the heater wire was identified. The downward motion of the heater wire deformed the vapor-liquid interface to nucleate the bubble-like embryo. The instability induced by fluid–solid coupling is the key mechanism for the nucleation of a bubble-like structure. Bubble-like nucleation is influenced by the thickness of the VL layer, the wire motion velocity, and the roughness of the VL interface. Because the newly created bubble-like structures are completely separated from the heater wire, the wettability and microcavities of the heater wire surface do not influence the bubble-like nucleation.

Bubble-like dynamics: Surface tension is critical in bubble dynamics under subcritical pressure conditions, but it becomes less significant in supercritical pressures. This results in three structures in the supercritical domain: a VL layer surrounding the wire, a bubble-like layer underneath the wire, and a plume above the wire. A steep density gradient is well established underneath the wire. The downward inertia force of the bubble-like interface competes with the upward buoyancy force to form a clear bubble-like interface. However, a gradual density gradient exists above the wire, resulting in the formation of a plume. Near the critical pressure, the surface tension is smaller by several orders of magnitude compared with that in subcritical pressures, but its existence is significant. The presence of surface tension in supercritical fluids is not yet fully understood [56]. The size of the bubble-like structure is approximately 100 μm (see Figs. 17–20), which is one order of magnitude smaller than the bubble size scaled as the capillary length l_{cl} at subcritical pressures [57]:

$$l_{cl} = \sqrt{\frac{\sigma}{\rho g}} \qquad (19)$$

where σ is the surface tension and ρ is the fluid density. The lifetime of a bubble is less than a few tens of milliseconds.
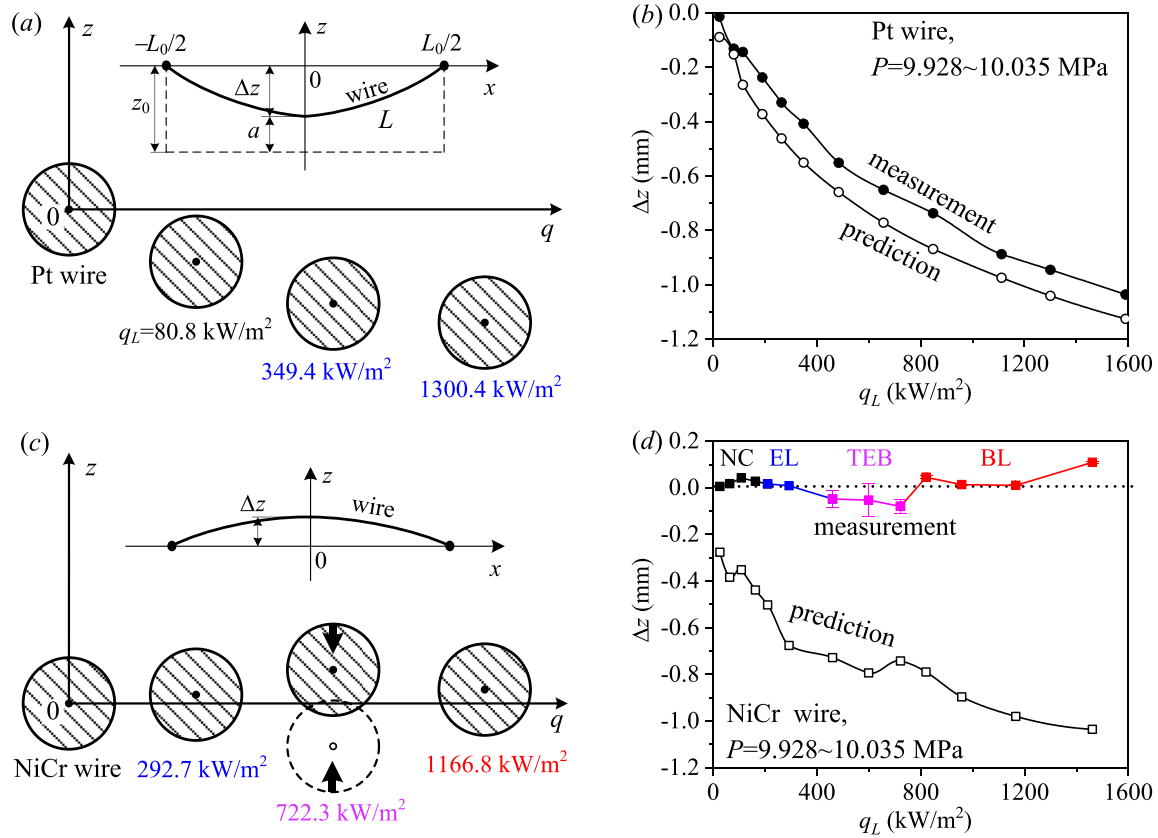
Fig. 21. Locations and displacements of two heater wires at P=10 MPa. (a) locations of the Pt wire at different heat fluxes q_L; (b) measured and predicted displacements of the Pt wire at different q_L; (c) locations of the NiCr wire at different heat fluxes q_L; (d) measured and predicted displacements of the NiCr wire at different q_L.

Boiling-like heat transfer mechanism: Heat transfer coefficients in the BL region are almost twice those in the EL region, indicating a significant enhancement in heat transfer (see Fig. 14c). In addition, heat transfer in the BL region displays random and disordered features (Fig. 19). The enhanced heat transfer and random features are similar to those of boiling under subcritical pressures, but the mechanisms deviate from those at subcritical pressures. Firstly, the current study identifies the self-sustained piston motion of the heater wire, creating a pumping effect to dissipate the generated VL layer and suck cold liquid towards the heater, which is distinct from the enhanced heat transfer at subcritical pressure. In contrast to the superheated liquid layer on the heater surface for subcritical boiling, a VL layer covers the heater wire in the supercritical domain. Transient thermal conduction occurs within the VL layer instead of the superheated liquid layer. Owing to the strong disturbance of the bubble-like interface, the interfacial heat transfer promotes heat and mass transfer, which is similar to the micro-convection mechanism during subcritical boiling.

5. Mechanism analysis for the observed phenomena

Here, the analysis aims to understand the reason for the different phenomena observed on the two wires.

5.1. Line expansion induced displacement of the wire

The two ends of the heater wire were fixed. The wire was straight in cold state but deformed under heating conditions. For the Pt wire, the downward bending was observed to ex-

hibit a larger displacement when the heat flux was increased (see Fig. 21a). The wire length changed from L_0 at cold temperature T_b to L at temperature $T_{w,L}$. L is expressed as

$$L = L_0 \alpha_L (T_{w,L} - T_b) \tag{20}$$

where α_L is the line-expansion coefficient of the wire. The Catenary equation gives L as follows [58]:

$$L = a\left(e^{\frac{L_0}{2a}} - e^{-\frac{L_0}{2a}}\right) \tag{21}$$

where a is the distance between the lowest point of the downward bending curve and the reference line, and z_0 is the vertical distance between the endpoint of the wire and the reference line (see Fig. 21a).

$$z_0 = \frac{a}{2}\left(e^{\frac{L_0}{2a}} + e^{-\frac{L_0}{2a}}\right) \tag{22}$$

$$\Delta z = z_0 - a \tag{23}$$

Eqs. (20)–(23) are used to calculate Δz by substituting $T_{w,L}$ at the corresponding q_L. The agreement between the predicted and measured displacements indicates a net downward force exerted on the Pt wire (Fig. 21b).

Upward bending existed for the NiCr wire, except for the piston motion with alternating upward and downward bending in the TEB region (see Fig. 21c). The catenary equation predicts a negative displacement of the NiCr wire (see Fig. 21d), which does not support the experimental results. The measurements yielded positive Δz results, indicating upward bending. In the TEB region, the error bars for each data point represent the amplitudes between the highest and lowest positions of the wire.
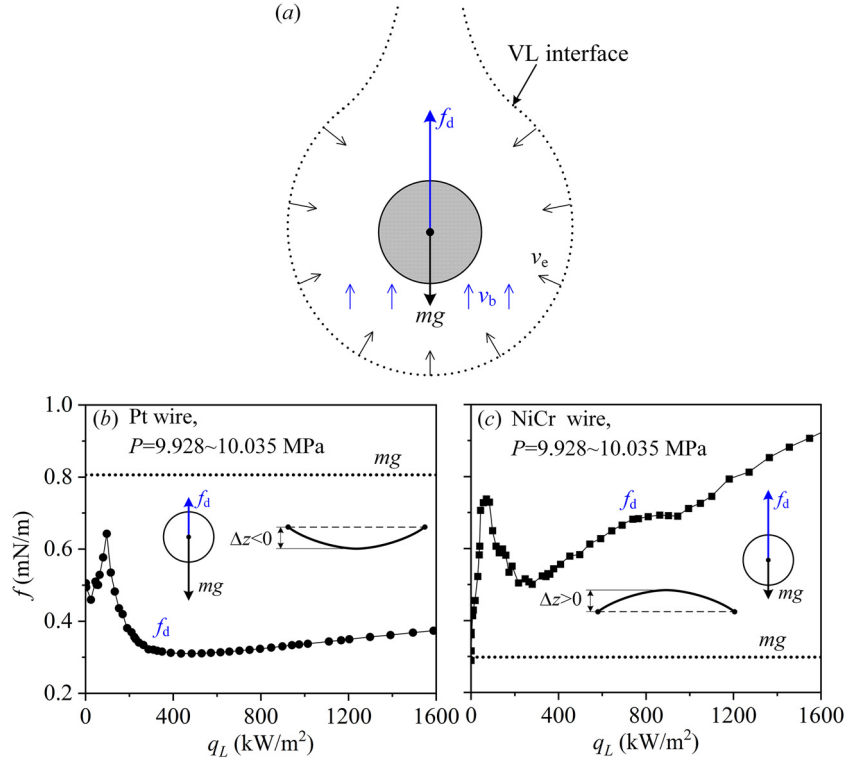
Fig. 22. Force balances between gravity and drag force for the two heater wires at $P=10$ MPa. (a) the model for the force analysis; (b) the competition between mg and f_d for the Pt wire; (c) the competition of mg and f_d for the NiCr wire.

5.2. Different bending direction of the two wires

For the NiCr wire, the deviation between predictions and measurements inspired us to perform a force analysis. Because the metal wire is one order of magnitude heavier than sCO$_2$, the buoyancy force F_b is temporarily neglected. Drag force F_d is caused by the natural convection induced buoyancy velocity v_b [59], as shown in Fig. 22(a).

$$v_b = [\alpha_T g \beta_T (T_{w,L} - T_b)]^{\frac{1}{3}} \qquad (24)$$

where α_T is the thermal diffusion coefficient, and β_T is the volume expansion coefficient of the fluid. Hence, the drag force per unit length of the wire f_d is

$$f_d = \frac{1}{2}\rho v_b^2 d C_d \qquad (25)$$

Considering a thin wire and a low Reynolds number Re, the drag coefficient C_d is [60]

$$C_d = \frac{8\pi Re}{\frac{1}{2} - \gamma - \ln\left(\frac{Re}{8}\right)} \qquad (26)$$

where $Re = \rho v_b d/\mu$, $\gamma = 0.577$ is the Eulerian coefficient, d is the wire diameter, and μ is the viscosity. Because α_T, β_T, ρ, and μ vary with T for sCO$_2$, the integration-averaging method quantifies the characteristic temperature for each physical property [61]:

$$\Phi_{int} = \frac{1}{T_{w,L} - T_b} \int_{T_b}^{T_{w,L}} \Phi(T) dT \qquad (27)$$

where Φ_{int} is the referenced thermal property.

Fig. 22(b) and (c) show the force balance between gravity and drag force versus heat fluxes at 10 MPa. A smaller f_d than mg indicates the downward bending of the Pt wire, whereas a larger f_d than mg indicates the upward bending of the NiCr wire, where m is the mass of the wire per unit length.

### 5.3. Piston motion induced intermittent boiling-like heat transfer

The drag force in Section 5.2 is estimated based on the single-phase fluid assumption. Interfacial expansion is used to explain the piston motion of the NiCr wire in the TEB region. Here, we examine the natural convection induced velocity boundary layer δ_v and the thermal boundary layer δ_{th} for a fluid heated by a horizontal cylinder (Fig. 23a). The magnitude of one boundary layer relative to the other depends on the Prandtl number Pr, as plotted in Fig. 23(b) for sCO$_2$ at 10 MPa. $Pr>1$ results in a thicker velocity boundary layer than the thermal boundary layer. At $T>110.8$°C, the Pr is smaller than 1 but does not deviate from 1 too much, under which δ_v is on the same magnitude with δ_{th}. Thus, the situation of $\delta_v > \delta_{th}$ was considered, noting the significant velocity and temperature gradients in each boundary layer (see Fig. 23a).

For simplification, pseudo-boiling is considered to have a VL interface, which is assumed to be located at the end of the thermal boundary layer (see Fig. 23a). At the VL interface, the evaporation from LL phase to VL phase forms an interfacial expansion velocity v_e. There are two effects of v_e. Firstly, evaporation momentum forces are created along the VL interface, whose total effect is zero for uniform evaporation around the wire [45]. Secondly, the existence of v_e is equivalent to injecting a hot fluid into the two boundary layers, ensuring that both boundary layers become thicker. Here, v_e is estimated as [54]

$$v_e = \frac{q_L}{\hbar_w - \hbar_b}\left(\frac{1}{\rho_w} - \frac{1}{\rho_b}\right) \qquad (28)$$

where $\hbar$ is the fluid enthalpy, and the subscripts w and b refer to the wall temperature and bulk fluid temperature conditions, respectively.

Fig. 23(c) shows v_b and v_e over the whole ranges of q_L for the NiCr wire, demonstrating a gentle rise in v_b but a linear rise in v_e. In the NC and EL regions, $v_e<0.5v_b$ causes a weak effect of
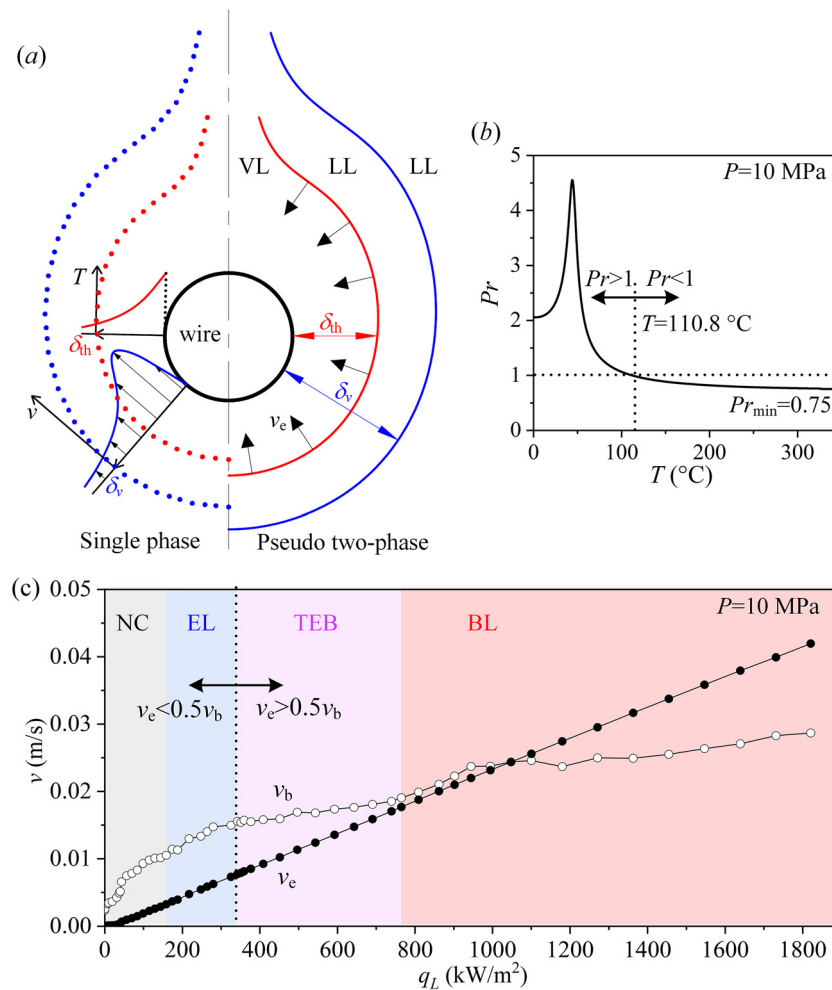
Fig. 23. Effect of interfacial expansion on drag force. (a) natural convection induced boundary layers without (left column) and with (right column) consideration of the interfacial evaporation. (b) The Pr number versus temperatures for 10 MPa sCO$_2$. (c) buoyance velocity v_b and expansion velocity v_e dependent on heat fluxes on the NiCr wire.

interfacial expansion on the drag force. A drag force larger than gravity causes the upward bending of the NiCr wire. In the TEB region, $v_e > 0.5v_b$ results in significant interfacial expansion of the drag force. This effect expands the velocity boundary layer to decrease the velocity gradients and weaken the drag force, explaining the change in the bending direction from upward to downward. The falling-down process of the NiCr wires has received significant attention. Taylor [62] commented on the interfacial instability in low-density fluids, such as gas penetrating high-density fluids such as liquids, which has nothing to do with surface tension. The larger the density difference, the more unstable the interface is. This theory is extended to supercritical pressures. During the fall of the NiCr wire, the penetration of a VL fluid into a LL fluid causes strong interfacial instability, triggering the nucleation and growth of bubble-like patterns. However, the bubble-like structures widen the thermal boundary layer to exceed the velocity boundary layer, under which v_e has a weak effect on the drag force. Hence, the drag force is recovered and pushes the wire upward. This process is repeated periodically to generate the piston motion of the NiCr wire.

In summary, the TEB region consists of substages of EL and BL; thus, it concerns intermittent BL heat transfer. During the falling of the wire, the penetration of lighter VL phase into heavier liquid-like phase causes the interfacial instability to form bubble-like patterns. Alternatively, enhanced and weakened inter-

facial expansions account for the piston motion of the heating wire.

5.4. Temporal-spatial temperature variation induced continuous boiling-like heat transfer

Instead of intermittent BL heat transfer in the TEB region, continuous BL heat transfer occurs in the BL region with the upward bending of the NiCr wire, indicating that the interfacial expansion velocity is equivalent to or larger than the buoyancy velocity ($v_e \sim v_b$ or $v_e > v_b$, see Fig. 23c). To explain the continuous BL heat transfer, the motionless wire state inspires us to seek a mechanism other than the lighter fluid penetrating the heavier fluid induced instability.

Referring to Fig. 24(a) and (b), following assumptions are made for the perturbation analysis of the VL film instability: (i) A uniform VL thickness exists over the circumference of the wire. (ii) The local wire temperatures T_w are functions of x and t, $T_w = T_w(x, t)$. The temperature variation in the radial direction, r, is neglected owing to the ultra-small Biot number. (iii) Although the electric resistance R and heat flux q are averaged over the entire heating length during experiment, they change locally versus x and time t: $R = R(x, t)$ and $q = q(x, t)$, respectively. (iv) Heat is transferred via the thermal conduction through VL layer but dissipates to surrounding liquid at the vapor–liquid interface owing to the
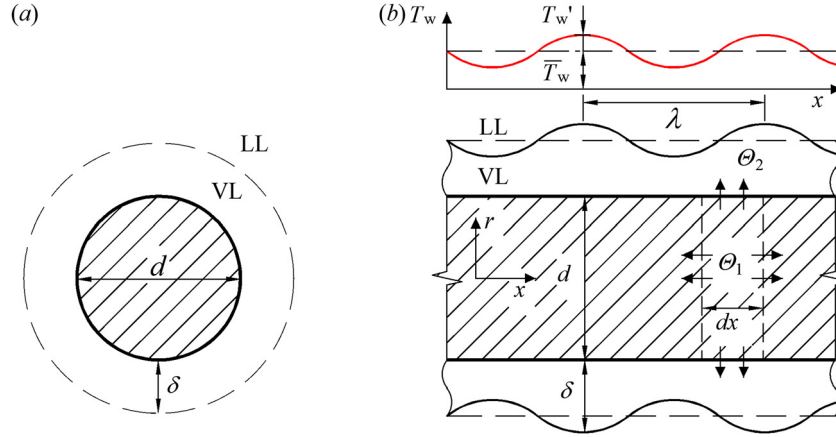
Fig. 24. Perturbation analysis for the spatial-time temperature variation induced BL heat transfer. (*a*) cross-sectional view of the model; (*b*) axial view of the model.

evaporation. The equation governing the spatial-time wire temperature is [44]

$$\rho_w c_{p,w} \frac{\partial T_w(x,t)}{\partial t} = \lambda_w \frac{\partial^2 T_w(x,t)}{\partial x^2} + \Theta_1(x,t) - \Theta_2(x,t) \qquad (29)$$

where c_p is the specific heat and the subscript w refers to the wire. Θ_1 is the heat source per unit volume of the wire owing to resistance heating, and Θ_2 is the heat dissipation per unit volume. The energy equations for the entire heater length L and microelement dx are as follows:

$$\begin{cases} q_L \pi \, dL = I^2 R_L = I^2 \bar{\rho}_0 (1 + j_T T_{w,L}) \frac{L}{s} \\ \Theta_1 s dx = I^2 R(x \to x + dx, t) = I^2 \bar{\rho}_0 (1 + j_T T_w) \frac{dx}{s} \end{cases} \qquad (30)$$

where q_L is the averaged heat flux across the length L, R_L is the total resistance of the heater, I is the current flowing through the wire, s is the cross-section area of the wire, j_T is the temperature coefficient of resistance, $\bar{\rho}_0$ is the resistivity at a reference temperature of 0°C. Eq. (30) gives

$$\Theta_1 = \frac{4 q_L (1 + j_T T_w)}{d(1 + j_T T_{w,L})} \qquad (31)$$

where $T_{w,L}$ is the temperature averaged over the wire length L. Thermal conduction in the VL layer yields

$$\Theta_2 = \frac{q \pi \, d dx}{s dx} = \frac{4}{d} \frac{\lambda_{VL}(T_w - T_{term})}{\delta} \qquad (32)$$

where λ_{VL} is the thermal conductivity of the VL layer, T_{term} is the temperature at the vapor–liquid interface, which is determined based on the thermodynamic approach for the termination temperature of pseudo-boiling [27].

The following non-dimensional parameters are introduced:

$$x^* = \frac{x}{d}, t^* = \frac{t}{\frac{\rho_w c_{p,w} d^2}{\lambda_w}}, T^* = \frac{T_w}{T_{term}}, \delta^* = \frac{\delta}{d} \qquad (33 \text{ a–d})$$

where $\frac{\rho_w c_{p,w} d^2}{\lambda_w}$ denotes the thermal diffusion time of the wire. Combining Eqs. (29), (31), (32) and (33) yields:

$$\frac{\partial T^*}{\partial t^*} = \frac{\partial^2 T^*}{\partial x^2} + \frac{4 q_L d j_T}{\lambda_w (1 + j_T T_{w,L})} T^* - \frac{4 \lambda_{VL}}{\lambda_w} \frac{T^* - 1}{\delta^*}$$
$$+ \frac{4 q_L d}{\lambda_w T_{term} (1 + j_T T_{w,L})} \qquad (34)$$

By introducing additional two dimensionless parameters of

$$H_1 = \frac{q_L d j_T}{\lambda_{VL}(1 + j_T T_{w,L})}, H_2 = \frac{\lambda_{VL}}{\lambda_w} \qquad (35)$$

Eq. (34) becomes

$$\frac{\partial T^*}{\partial t^*} = \frac{\partial^2 T^*}{\partial x^{*2}} + 4 H_1 H_2 T^* - 4 H_2 \frac{T^* - 1}{\delta^*} + \frac{H_1 H_2}{j_T T_{term}} \qquad (36)$$

In this study, the VL film thickness was δ, obtained from the measurement data of sCO$_2$. The last term on the right side of Eq. (36) is constant. The relationship between T^* and δ^* is correlated based on the measured $T_{w,L}$ and δ for each Pt and NiCr wire.

$$\frac{T^* - 1}{\delta^*} = c_1 T^{*2} + c_2 T^* + c_3 \qquad (37)$$

The constants c_1, c_2 and c_3 for the Pt and NiCr wires will be discussed later. Eq. (36) becomes

$$\frac{\partial T^*}{\partial t^*} = \frac{\partial^2 T^*}{\partial x^{*2}} - 4 c_1 H_2 T^{*2} + 4(H_1 - c_2) H_2 T^* - 4 c_3 H_2 + \frac{H_1 H_2}{j_T T_{term}}$$
$$(38)$$

The small-perturbation theory treats T^* as a steady $\bar{T}^*$ that is independent of x and t, plus a perturbation $T^{*\prime}$ [37]. Hence

$$T^*(x^*, t^*) = \bar{T}^* + T^{*\prime} \qquad (39)$$

The perturbation term is expressed as the simple harmonic form as

$$T^{*\prime} = A_\Psi^* e^{ik^* x^*} e^{\zeta t^*} \qquad (40)$$

where A_Ψ^* is the non-dimensional amplitude, k^* is the non-dimensional wave number related to the wave number k as $k^* = kd$, and ζ is the non-dimensional perturbation propagation velocity. A system is stable if $\zeta < 0$, but becomes unstable when $\zeta > 0$. Substituting Eqs. (39) and (40) into Eq. (38), the derivation of the equation with respect to time t yields

$$\zeta = H_3 - k^{*2} \qquad (41)$$

where $H_3 = 4 H_2 (H_1 - c_2 - 2 c_1 \bar{T}^*)$ and $\bar{T}^*$ are the steady values at x, that is $\bar{T}^* = T_{w,L}^* = T_{w,L}/T_{term}$, and $T_{w,L}$ is experimentally determined, noting that products of the high-order perturbation quantities are neglected.

Physically, H_1 represents the effect of temperature coefficient of resistance j_T on temperature perturbations. A larger j_T of the wire may result in a larger temperature perturbation. H_2 represents the thermal conductivity of the VL film relative to that of the wire. A larger H_2 implies enhanced thermal conduction in the VL layer relative to the wire, resulting in stronger non-uniformity along x and a larger perturbation versus t. Note that $\zeta > 0$ is the criterion for an oscillating system. Because the non-dimensional wave number k^* can take any value, the necessary condition for the perturbation is
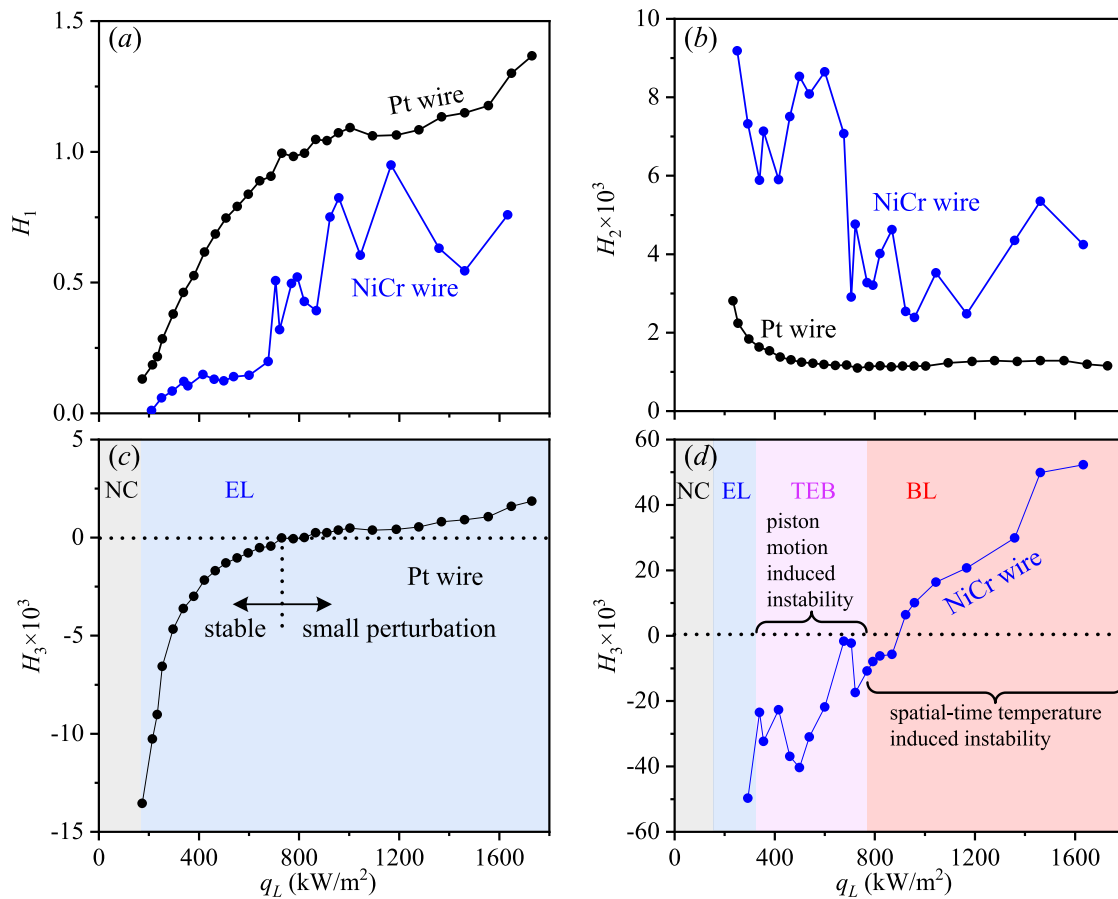
Fig. 25. Non-dimensional number versus q_L of Pt and NiCr wire at $P=10$ MPa. (a) H_1; (b) H_2; (c) and (d) H_3.

$H_3 > 0$, under which the T_w oscillation increases with an increase in H_3.

Here, we comment on the perturbation analysis at $T_{term} = 85.5°C$ for 10 MPa sCO$_2$. The thermal conductivity λ_{VL} in Eq. (35) varies with temperatures. The calibration value of λ_{VL} is obtained from the heat conduction between the wire and the VL layer in cylindrical coordinates as follows:

$$\lambda_{VL} = \frac{q_L d}{2(T_{w,L} - T_{term})} \ln\left(\frac{d + 2\delta}{d}\right) \qquad (42)$$

In Eq. (37), the three coefficients are well correlated based on the measured $T_{w,L}$ and δ, which are $c_1 = -0.00345$, $c_2 = 1.0291$, and $c_3 = -0.6147$ for the Pt wire, and $c_1 = -0.8592$, $c_2 = 4.8468$, and $c_3 = -4.0528$ for the NiCr wire. Fig. 25(a) plots H_1 with $j_T = 3.85 \times 10^{-3}$K^{-1} and 4.22×10^{-4}K^{-1} for the Pt and NiCr wires, respectively, indicating a much larger H_1 for the Pt wire than that for the NiCr wire. It appears that the wire temperature is more likely to oscillate for the Pt wire than those for the NiCr wire, which is contrary to our experiment where only the EL mode occurs for the Pt wire. The NiCr wire had a much larger H_2 than the Pt wire (see Fig. 25b). The NiCr wire is more likely to exhibit temperature oscillations than the Pt wire, which is consistent with our measurements.

Because H_1 and H_2 are non-dimensional parameters in Eq. (38) and not a result of perturbation analysis, the stability characteristic cannot be solely determined based on H_1 or H_2. H_3 is derived after the perturbation analysis and is related to H_1, H_2, c_1, and c_2; hence, it is a comprehensive index for verifying the stability of the thermal system. The variations in H_3 depending on heat fluxes at 10 MPa are presented in Fig. 25(c) and (d) for both wires.

For the Pt wire, a negative H_3 value when $q_L < 730.7$ kW/m^2 indicates a stable system. As q_L exceeds 730.7 kW/m^2, H_3 for the Pt wire becomes positive, but is still ∼30 times smaller than that of the NiCr wire. The positive but small H_3 (10^{-3} magnitude) explains the EL mode only with minimal variations in the wire temperatures, as shown in Fig. 13, but it is not sufficient to trigger the BL mode over the entire heat flux range.

For the NiCr wire, H_3 in the TEB region is negative, further supporting the fact that the intermittent BL heat transfer is caused by the dynamic wire motion, instead of the temporal-spatial wire temperatures. In the BL region, the majority of H_3 data points are positive and exhibit a sharp increase with q_L. The maximum value of H_3 reaches 52.3, except for four negative H_3 data points just beyond the TEB region. This variation trend of H_3 over the entire heat flux range proves that the intermittent BL heat transfer is caused by the piston motion of the wire in the TEB region, and the continuous BL heat transfer is indeed caused by temporal-spatial temperature variations.

5.5. Comparison with other studies

In this study, supercritical heat transfer is investigated and quantitatively characterized. Except the NC mode, the EL mode is observed for the Pt wire, but the modes of EL, TEB and BL are observed for the NiCr wire. Intermittent boiling-like heat transfer occurs in the TEB region and continuous boiling-like heat transfer occurs in the BL region. The former is caused by the piston motion induced instability, and the latter is induced by the spatial-temporal temperature variations of the wire. Knapp & Sabersky [20] identified laminar flow, oscillation flow and bubble-like flow

in supercritical pressures. The oscillation flow and bubble-like flow are similar to the TEB flow and BL flow reported in this study. Knapp and Sabersky [20] mixed the NC flow and the EL flow as the laminar flow. Actually, the NC mode and the EL mode are quite different, because NC belongs to the single-phase heat transfer, but the EL heat transfer belongs to the phase change. The shadow method used in Ref. [20] amplifies the density gradient of the flow field. The recorded images were blurry to identify the vapor-liquid interface during pseudo-boiling. In this study, the direct photograph technique clearly captures the pseudo-boiling interface, thus quantitative tracking of the pseudo-boiling interface becomes possible.

Different phenomena were reported for supercritical heat transfer using the Pt wire and the NiCr wire. Hahne & Neumann [21,22] observed bubble-like structure using the NiCr wire, but such phenomenon was not observed using the Pt wire. This difference was commented to be caused by the surface roughness, temperture coefficient of reistence, thermal conductivity and thermal diffusion coefficient of the wire. Here, the intermittent boiling-like heat transfer is caused by the pistion motion of the wire, and the continuous boiling-like heat transfer is caused by the spatial-temporal temperature variations of the wire.

In supercritical pressures, the vapor-liquid layer thickness is never reported previously, but it is quantified experimentally in this study. Because the EL heat transfer in supercritical pressures can be analogized to film boiling in subcritical pressures, we extend the film thickness in subcritical pressures to estimate the values in supercritical pressures. Sarma et al. [63] established the model for film boiling on horizontal cylinder in subcritical pressures. The model assumes larger diameter of the cylinder, thus the surface tension force and the axial flow can be neglected. The heat transfer rate due to thermal conduction across the vapor-liquid layer equals to that due to evaporation at the vapor-liquid interface. Sarma et al. [63] developed δ_{sub} as

$$\delta_{sub} = 1.56 \left[\frac{\lambda_v \mu_v d(T_w - T_s)}{g(\rho_l - \rho_v)(\hbar_v - \hbar_l)} \right]^{\frac{1}{4}} \tag{43}$$

Where the subscripts l and v represent liquid and vapor, respectively, λ is the thermal conductivity, μ is the viscosity and T_s is the saturation temperature and $\hbar$ is the enthalpy.

In supercritical pressures, T_{start} and T_{term} are used to quantify the LL and VL temperature, respectively, in which T_{start} and T_{term} are determined by Ref. [27]. Eq. (43) is modified to estimate the VL layer thickness δ_{sup} as

$$\delta_{sup} = 1.56 \left[\frac{\lambda_{term} \mu_{term} d \Delta T_{w,L}}{g(\rho_{start} - \rho_{term})(\hbar_{term} - \hbar_{start})} \right]^{\frac{1}{4}} \tag{44}$$

Fig. 26 presents the comparison between the measured VL layer thickness and the predictions using Eq. (44), using the Pt wire at 10 MPa pressure and 15 °C bulk liquid temperature. Good agreement is achieved between the measured values and the calculated values, with the average relative deviation of 17.3%.

Finally, we further emphasize the two modes of heat transfer. In subcritical pressures, evaporation takes place at the existing vapor-liquid interface, but boiling involves the creation of new vapor-liquid interfaces [33]. Evaporation either occurs with the same substance of the working fluid, or occurs with different substances of the working fluids. Ref. [7] writes "*Evaporation occurs at the liquid–vapor interface when the vapor pressure is less than the saturation pressure of the liquid at a given temperature*". There are two necessary conditions for evaporation to take place: (1) there exists vapor-liquid interface, and (2) the vapor pressure is smaller than the saturation pressure. Evaporation of water in a glass bottle involves two substances of water and air, under which evaporation is caused by the mass transfer from liquid to vapor within a mixed
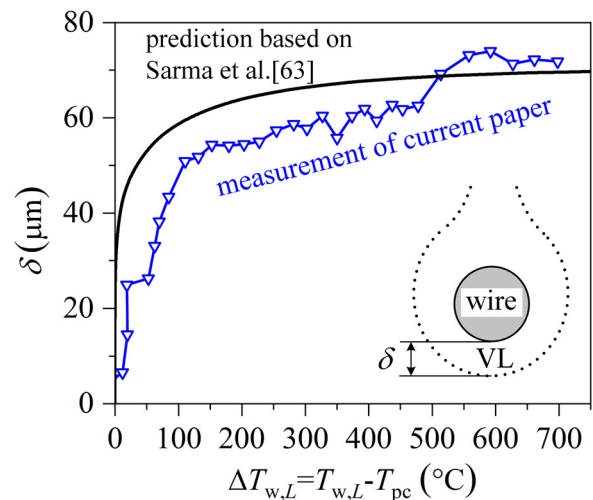

Fig. 26. Comparison of the VL thickness δ at the bottom of the wire measured in this paper on Pt wire with P=10 MPa and the predictions based on Sarma et al. [63].

gas layer (air and vapor). Alternatively, evaporation widely takes place in heated tubes for annular flow, in which the liquid layer may be thin enough to keep the wall temperature below the nucleation temperature [64]. Evaporation does happen instead of boiling. The evaporation involves the phase change with a single substance of liquid such as water instead of multi-species of working fluids. In this work, the two modes of EL and BL in supercritical pressures are analogized to evaporation and boiling in subcritical pressures, respectively.

6. Conclusions

Evaporation and boiling are two heat transfer modes in subcritical pressures; the former occurs on the existing vapor–liquid interface, whereas the latter creates new vapor–embryo interface. It is unclear whether these two heat transfer modes occur in supercritical pressures. If so, what are the triggering mechanisms? To answer these questions, elaborate experiments are performed using thin metal wires as heaters and temperature sensors. Throughout the experiment, the sCO_2 temperature remains at 15°C while the pressure is maintained at either 8 MPa or 10 MPa, both of which exceed the critical pressure of CO_2, which is 7.377 MPa.

Instead of the schlieren or shadowgraph method, a direct photograph technique was developed to track the bubble-like dynamics under supercritical pressure, avoiding the loss of light brightness. The light-refractive principle helps analyse the brighter/darker patterns during pseudo-boiling. The grey extraction method tracks the vapor–liquid interface and determines the thickness of the VL layer. A fibre optic detects the local temperature with high time resolution. The synchroniser coordinates all the systems together for comprehensive measurements.

It is found that the NC mode and EL mode appear consecutively with increase in heat fluxes for the Pt wire. In contrast, there are four modes for the NiCr wire: NC mode, EL mode, TEB mode, and BL mode. Different fluid-solid couplings induce different phenomena on the heater wires. The downward bending of the Pt wire can be attributed to gravity being greater than the drag force acting on the wire. In contrast, the upward bending of the NiCr wire is a result of the opposite phenomenon, where the drag force is greater than the gravity.

When Pr>1 or Pr~1 for sCO_2, the thermal boundary layer lies inside the velocity boundary layer; thus, the interfacial expansion velocity influences the velocity gradient to alter the drag force. A

TEB cycle consists of an EL stage and a BL stage. During the upward motion of the EL stage, the interfacial expansion effect is stronger to decrease the drag force; however, during the downward motion of the BL stage, the interfacial expansion effect is weakened to recover the drag force. Hence, the motion direction is periodically changed to form the piston motion of the wire. Owing to the instability induced by the penetration of lighter fluid into heavier fluid, the bubble-like structure nucleates, grows, and collapses.

Continuous BL heat transfer takes place at sufficiently high heat fluxes. Small-perturbation analysis provides a new non-dimensional parameter, H_3. For the Pt wire, a smaller H_3 (either negative or positive) explains only the EL mode. For the NiCr wire, the negative H_3 in the TEB region proves that the intermittent boiling-like heat transfer is caused by the piston motion of the wire, but the positive and ~30 times larger H_3 indicates that the continuous boiling-like heat transfer is caused by the temporal-spatial temperature variations.

The BL heat transfer is observed to occur on the basis of a VL layer, which differs from subcritical boiling. Due to sharp density gradient underneath the heater, the BL heat transfer occurs there. Because the BL process is related to interfacial instability, transient thermal conduction occurs in the VL film instead of at the superheated liquid layer in subcritical pressures. The bubble-like patterns severely disturb the flow field to create strong microconvection at the vapor-liquid interface, accounting for enhanced heat transfer. The BL heat transfer possesses random and disordered features similar to those of subcritical boiling. This study enhances the understanding of bubble-like dynamics during pseudo-boiling in supercritical pressures.

Declaration of Competing Interest

The authors declare that they have no known competing financial interests or personal relationships that could have appeared to influence the work reported in this paper.

CRediT authorship contribution statement

Xiaotian He: Methodology, Software, Validation, Formal analysis, Investigation, Writing – review & editing. **Jinliang Xu:** Conceptualization, Writing – original draft, Supervision. **Xiongjiang Yu:** Resources. **Jian Xie:** Project administration.

Data availability

Data will be made available on request.

Acknowledgments

Supplementary materials

Supplementary material associated with this article can be found, in the online version, at doi:10.1016/j.ijheatmasstransfer.2023.124417.

References

[1] R.M. Smith, Nomenclature for supercritical fluid chromatography and extraction (IUPAC Recommendations 1993), Pure Appl. Chem. 65 (11) (1993) 2397–2403.

[2] V. Dostal, P. Hejzlar, M.J. Driscoll, The supercritical carbon dioxide power cycle: comparison to other advanced power cycles, Nucl. Technol. 154 (3) (2006) 283–301.

[3] J. Guo, M. Li, J. Xu, J. Yan, T. Ma, Energy, exergy and economic (3E) evaluation and conceptual design of the 1000 MW coal-fired power plants integrated with S-CO2 Brayton cycles, Energy Convers. Manage. 211 (2020) 112713.

[4] O. Catchpole, N. Perry, B. Da Silva, J. Grey, B. Smallfield, Supercritical extraction of herbs I: Saw Palmetto, St John's wort, Kava root, and Echinacea, J. Supercrit. Fluids 22 (2) (2002) 129–138.

[5] E. Reverchon, R. Adami, Nanomaterials and supercritical fluids, J. Supercrit. Fluids 37 (1) (2006) 1–22.

[6] A.A. Peterson, F. Vogel, R.P. Lachance, M. Fröling, M.J. Antal Jr, J.W. Tester, Thermochemical biofuel production in hydrothermal media: a review of sub-and supercritical water technologies, Energy Environ. Sci. 1 (1) (2008) 32–65.

[7] Y. Cengel, M. Boles, Thermodynamics: An Engineering Approach, 6th ed., Mc-Graw-Hill Companies, (SI Units)New York, 2007.

[8] J. Jackson, W. Hall, Influences of buoyancy on heat transfer to fluids flowing in vertical tubes under turbulent conditions, in: Turbulent Forced Convection in Channels and Bundles, Hemisphere Publishing Corporation, 1979, pp. 613–640.

[9] J. Yu, B. Jia, D. Wu, D. Wang, Optimization of heat transfer coefficient correlation at supercritical pressure using genetic algorithms, Heat Mass Transfer 45 (6) (2009) 757–766.

[10] J. Jackson, Fluid flow and convective heat transfer to fluids at supercritical pressure, Nucl. Eng. Des. 264 (2013) 24–40.

[11] I.L. Pioro, H.F. Khartabil, R.B. Duffey, Heat transfer to supercritical fluids flowing in channels—empirical correlations (survey), Nucl. Eng. Des. 230 (1-3) (2004) 69–91.

[12] J. Xu, C. Liu, E. Sun, J. Xie, M. Li, Y. Yang, J. Liu, Perspective of S− CO2 power cycles, Energy 186 (2019) 115831.

[13] M. Pizzarelli, The status of the research on the heat transfer deterioration in supercritical fluids: a review, Int. Commun. Heat Mass Transf. 95 (2018) 132–138.

[14] B. Zhu, J. Xu, H. Zhang, J. Xie, M. Li, Effect of non-uniform heating on scCO2 heat transfer deterioration, Appl. Therm. Eng. 181 (2020) 115967.

[15] N. Kafengauz, M. Fedorov, Excitation of high-frequency pressure oscillations during heat exchange with diisopropylcyclohexane, J. Eng. Phys. 11 (1) (1966) 63–67.

[16] N. Kafengauz, M. Fedorov, Pseudoboiling and heat transfer in a turbulent flow, J. Eng. Phys. 14 (5) (1968) 489–490.

[17] Q. Zhang, H. Li, X. Lei, J. Zhang, X. Kong, Study on identification method of heat transfer deterioration of supercritical fluids in vertically heated tubes, Int. J. Heat Mass Transfer 127 (2018) 674–686.

[18] G.A. Schatte, A. Kohlhepp, C. Wieland, H. Spliethoff, Development of a new empirical correlation for the prediction of the onset of the deterioration of heat transfer to supercritical water in vertical tubes, Int. J. Heat Mass Transfer 102 (2016) 133–141.

[19] K. Goldmann, Heat transfer to supercritical water at 5000 psi flowing at high mass flow rates through round tubes, Int. Devel. Heat Transf. 3 (1961) 561–568.

[20] K.K. Knapp, R.H. Sabersky, Free convection heat transfer to carbon dioxide near the critical point, Int. J. Heat Mass Transf. 9 (1) (1966) 41–51.

[21] E. Hahne, R. Neumann, Boiling-like phenomena in free-convection heat transfer at supercritical pressures, Wärme-und Stoffübertragung 15 (3) (1981) 171–180.

[22] R.J. Neumann, E.W. Hahne, Free convective heat transfer to supercritical carbon dioxide, Int. J. Heat Mass Transf. 23 (12) (1980) 1643–1652.

[23] J. Tamba, T. Takahashi, T. Ohara, T. Aihara, Transition from boiling to free convection in supercritical fluid, Exp. Therm Fluid Sci. 17 (3) (1998) 248–255.

[24] J. Tamba, T. Ohara, T. Aihara, MD study on interfacelike phenomena in supercritical fluid, Microscale Thermophys. Eng. 1 (1) (1997) 19–30.

[25] B. Widom, Equation of state in the neighborhood of the critical point, J. Chem. Phys. 43 (11) (1965) 3898–3905.

[26] P. Gallo, D. Corradini, M. Rovere, Widom line and dynamical crossovers as routes to understand supercritical water, Nat. Commun. 5 (1) (2014) 1–6.

[27] D. Banuti, Crossing the Widom-line–supercritical pseudo-boiling, J. Supercrit. Fluids 98 (2015) 12–16.

[28] F. Maxim, C. Contescu, P. Boillat, B. Niceno, K. Karalis, A. Testino, C. Ludwig, Visualization of supercritical water pseudo-boiling at Widom line crossover, Nat. Commun. 10 (1) (2019) 1–11.

[29] F. Maxim, K. Karalis, P. Boillat, D.T. Banuti, J.I. Marquez Damian, B. Niceno, C. Ludwig, Thermodynamics and dynamics of supercritical water pseudo-boiling, Adv. Sci. 8 (3) (2021) 2002312.

[30] M.Y. Ha, T.J. Yoon, T. Tlusty, Y. Jho, W.B. Lee, Widom delta of supercritical gas–liquid coexistence, J. Phys. Chem. Lett. 9 (7) (2018) 1734–1738.

[31] J. Xu, Y. Wang, X. Ma, Phase distribution including a bubblelike region in supercritical fluid, Phys. Rev. E 104 (1) (2021) 014142.

[32] K. Nishikawa, T. Ito, H. Yamashita, Free-convective heat transfer to a supercritical fluid, J. Heat Transf. 95 (2) (1973) 187–191.

[33] S. Kandlikar, M. Shoji, V. Dhir, Handbook of Phase Change: Boiling and Condensation, Talyor & Francis, Philadelphia, 1999.

[34] S. Hussain, A. Haji-Akbari, Studying rare events using forward-flux sampling: Recent breakthroughs and future outlook, J. Chem. Phys. 152 (6) (2020) 060901.

[35] International Electrotechnical Commission, Industrial platinum resistance thermometers and platinum temperature sensorsInternational Standard IEC, IEC, 2008.

[36] M.V. Avdeev, A.N. Konovalov, V.N. Bagratashvili, V.K. Popov, S.I. Tsypina, M. Sokolova, J. Ke, M. Poliakoff, The fibre optic reflectometer: a new and simple probe for refractive index and phase separation measurements in gases, liquids and supercritical fluids, PCCP 6 (6) (2004) 1258–1263.

[37] V.P. Carey, Liquid-Vapor Phase-Change Phenomena: An Introduction to the Thermophysics of Vaporization and Condensation Processes in Heat Transfer Equipment, 3rd ed., CRC Press, Boca Raton, 2020.

[38] D. Estruch, N. Lawson, D. MacManus, K. Garry, J. Stollery, Measurement of shock wave unsteadiness using a high-speed schlieren system and digital image processing, Rev. Sci. Instrum. 79 (12) (2008) 126108.

[39] H.S. Sim, N. Maes, L. Weiss, L.M. Pickett, S.A. Skeen, Detailed measurements of transient two-stage ignition and combustion processes in high-pressure spray flames using simultaneous high-speed formaldehyde PLIF and schlieren imaging, Proc. Combust. Inst. 38 (4) (2021) 5713–5721.

[40] B. Yu, X. He, J. Xu, Experiment and numerical simulation of supercritical CO2 pool heat transfer (in Chinese), Scientia Sinica Technol. (2022), doi:10.1360/SST-2022-0325.

[41] A. Hunter, P. Schreiber, Mach-Zehnder interferometer data reduction method for refractively inhomogeneous test objects, Appl. Opt. 14 (3) (1975) 634–639.

[42] P.M. Tripathi, S. Basu, Insights into the dynamics of supercritical water flow using a two-phase approach, Phys. Fluids 33 (4) (2021) 043304.

[43] J.P. Holman, Experimental Methods for Engineers, McGraw-Hill, New York, 2012.

[44] Y. Cengel, Heat and Mass Transfer A Practical Approach, McGraw-Hill Companies, New York, 2006.

[45] B. Zhu, J. Xu, C. Yan, J. Xie, The general supercritical heat transfer correlation for vertical up-flow tubes: K number correlation, Int. J. Heat Mass Transf. 148 (2020) 119080.

[46] P. Githinji, R. Sabersky, Some effects of the orientation of the heating surface in nucleate boiling, J. Heat Transf. 85 (1963) 379.

[47] L. Mao, W. Zhou, X. Hu, Y. He, G. Zhang, L. Zhang, R. Fu, Pool boiling performance and bubble dynamics on graphene oxide nanocoating surface, Int. J. Therm. Sci. 147 (2020) 106154.

[48] H. Nemati, A. Patel, B.J. Boersma, R. Pecnik, The effect of thermal boundary conditions on forced convection heat transfer to fluids at supercritical pressure, J. Fluid Mech. 800 (2016) 531–556.

[49] J. Ren, O. Marxen, R. Pecnik, Boundary-layer stability of supercritical fluids in the vicinity of the Widom line, J. Fluid Mech. 871 (2019) 831–864.

[50] M. Shoji, Studies of boiling chaos: a review, Int. J. Heat Mass Transf. 47 (6-7) (2004) 1105–1128.

[51] J.R. Patrick-Yeboah, R.C. Reid, Superheat-limit temperatures of polar liquids, Ind. Eng. Chem. 20 (4) (1981) 315–317.

[52] R. Cole, in: Boiling Nucleation, in: Advances in Heat Transfer, Elsevier, 1974, pp. 85–166.

[53] B. Mikic, W. Rohsenow, A new correlation of pool-boiling data including the effect of heating surface characteristics, J. Heat Transf. 91 (2) (1969) 245–250.

[54] S. Kandlikar, Controlling bubble motion over heated surface through evaporation momentum force to enhance pool boiling heat transfer, Appl. Phys. Lett. 102 (5) (2013) 051611.

[55] M.K. Gupta, D.S. Sharma, V.J. Lakhera, Vapor bubble formation, forces, and induced vibration: a review, Appl. Mech. Rev. 68 (3) (2016) 030801.

[56] Q. Wang, X. Ma, J. Xu, M. Li, Y. Wang, The three-regime-model for pseudo-boiling in supercritical pressure, Int. J. Heat Mass Transf. 181 (2021) 121875.

[57] D. Aarts, Capillary length in a fluid− fluid demixed colloid− polymer mixture, J. Phys. Chem. B 109 (15) (2005) 7407–7411.

[58] J. Kacmarynski, The Catenary, State University of Iowa, 1931.

[59] A. Liñán, V.N. Kurdyumov, Laminar free convection induced by a line heat source, and heat transfer from wires at small Grashof numbers, J. Fluid Mech. 362 (1998) 199–227.

[60] H. Lamb, Hydrodynamics, University Press, 1924.

[61] H. Kato, N. Nishiwaki, M. Hirata, Studies on the heat transfer of fluids at a supercritical pressure: 1st report, a proposition of reference values of thermal properties and experiments with supercritical carbon-dioxide, Bull. JSME 11 (46) (1968) 654–663.

[62] G.I. Taylor, The instability of liquid surfaces when accelerated in a direction perpendicular to their planes. I, Proc. R. Soc. Lond. A 201 (1065) (1950) 192–196.

[63] P.K. Sarma, T. Subrahmanyam, V.D. Rao, A.E. Bergles, Turbulent film boiling on a horizontal cylinder, Int. J. Heat Mass Transf. 44 (1) (2001) 207–214.

[64] W.M. Rohsenow, Boiling, Annu. Rev. Fluid Mech. 3 (1) (1971) 211–236.